Supporting Information

Active site proximity regulates selectivity in ammonia oxidation reactions

Yan Wang[1], Polina Lavrik[1], Shouwei Zuo[2], Teng Li[1], Mohamad Abou-Daher[1,3], Sarah Komaty Zaarour[1], Abdallah Nassereddine[4], Antonio Aguilar-Tapia[4], Abdul-Hamid Emwas[5], Jean-Louis Hazemann[4], Aamir Farooq[3], Huabin Zhang[2], Javier Ruiz-Martínez[1*]

[1]: Catalysis, Nanomaterials and Spectroscopy (CNS) Group, KAUST Catalysis Center (KCC), King Abdullah University of Science and Technology, Thuwal, 23955, Saudi Arabia; Physical Science and Engineering (PSE) Division, King Abdullah University of Science and Technology, Thuwal 23955, Saudi Arabia

[2]: Advanced Catalysis of Sustainable Energy (ACSE) Group, KAUST Catalysis Center (KCC), King Abdullah University of Science and Technology, Thuwal, 23955, Saudi Arabia; Physical Science and Engineering (PSE) Division, King Abdullah University of Science and Technology, Thuwal 23955, Saudi Arabia

[3]: Farooq's group for Advanced Sensing Technology & Energy Research (FASTER), Clean Energy Research Platform (CERP), King Abdullah University of Science and Technology, Thuwal, 23955, Saudi Arabia; Physical Science and Engineering (PSE) Division, King Abdullah University of Science and Technology, Thuwal 23955, Saudi Arabia

[4]: Institut de Chimie Moléculaire de Grenoble, UAR2607 CNRS Université Grenoble Alpes, F-38000, Grenoble, France

[5]: Core Labs, King Abdullah University of Science and Technology (KAUST), 23955-6900, Thuwal, Kingdom of Saudi Arabia

Table of Contents

Supplementary Note 1. Catalyst synthesis and basic characterization

Catalyst synthesis

To synthesize Mn single sites supported on TiO_2, layered protonated titanates (LPTs) with a zeta potential of -3.09 mV were used as the starting support. Then, the support is impregnated with a manganese acetate solution in ethanol, which has a zeta potential of 3.72 mV (**Supplementary Table 2**). This ensures strong electrostatic adsorption and a high dispersion of the manganese acetate precursor on the LPTs surface. In the case of the supported nanocluster synthesis, the LPTs support was previously calcined at 450 ^{o}C (**Supplementary Fig. 1**). This results in a change in the zeta potential of the support to a positive value (0.81 mV) due to the phase transformation from LPTs to anatase, as confirmed by *in situ* XRD measurements of the calcination process (**Supplementary Fig. 2**). As a consequence of the weak precursor / support interaction, the MnO_x species have a larger tendency to agglomerate, hence for the Mn nanoclusters synthesis, the calcined LPTs was used as the support for further impregnation with same amount of Mn acetate.

Basic characterization

The interaction between Mn atom and LPTs influenced the crystallinity of TiO_2 during calcination, this is evident from the lower XRD peak intensities observed in the 2SS sample compared to 2NP, as the diffraction pattern of the pure SS support closely resembles that of the NP support (**Supplementary Fig. 3**). The gradual reduction in diffraction peak intensities with increasing Mn loading in SS samples suggests that MnO_x doping disrupts crystal symmetry, leading to shifts in the two theta angles. In contrast, this phenomenon is not observed in 2NP, indicating that this impregnation method does not significantly affect the anatase structure. Additional structural insight was provided by UV-Vis spectroscopy. The absorption spectra of the support and NP samples closely resemble that of pure anatase TiO_2 (**Supplementary Fig. 4a**), suggesting weak interaction between the Mn phase and the support. In SS samples, the absorption band broadens toward higher wavelengths with increasing Mn content, which can be explained by substitution of Ti^{4+} by Mn cations[1]. Raman spectroscopy reveals only bands corresponding to TiO_2 anatase across all samples (**Supplementary Fig. 4b**). The most intense E_g (1) Raman mode at 143 cm^{-1} is attributed to symmetric O-Ti-O stretching and is highly sensitive to the local oxygen environment surrounding Ti^{4+} [2]. The addition of Mn on the support results in a blue shift of the E_g band, suggesting a loss in the lattice symmetry due to the incorporation of Mn cations. This shift is more pronounced in the SS samples compared to the NP ones, indicating for formation of more Mn-O-Ti bonds in the SS samples. Hence, both results from UV-Vis and Raman spectra suggest that Mn-O-Ti structure are more prevalent in SS samples, while NP samples likely contain a mixture of Mn-O-Ti and more Mn-O-Mn structures, associated with MnO_x clustering.

ICP-OES

Supplementary Table 1. ICP-OES results for Mn SS, Mn NP, Ni SS, Ni NP, Co SS and Co NP samples used in this work.

Sample	Mn / wt %	Ni / wt %	Co / wt %
1SS	0.97	-	-
1NP	0.89	-	-
2SS	1.99	-	-
2NP	1.94	-	-
6SS	5.57	-	-
6NP	5.93	-	-
2Ni SS	-	2.26	-
2Ni NP	-	2.20	-
6Ni SS	-	5.75	-
6Ni NP	-	5.71	-
2Co SS	-	-	2.28
2Co NP	-	-	2.18
6Co SS	-	-	5.90
6Co NP	-	-	5.83

Zeta potential

Supplementary Table 2. The zeta potential values of LPTs, Mn salt and Calcined LPTs.

Sample	Zeta potential (mV)
Layered Protonated Titanates (LPTs)	-3.09
Manganese (II) acetate tetrahydrate	3.72
Calcined LPTs	0.81

TGA

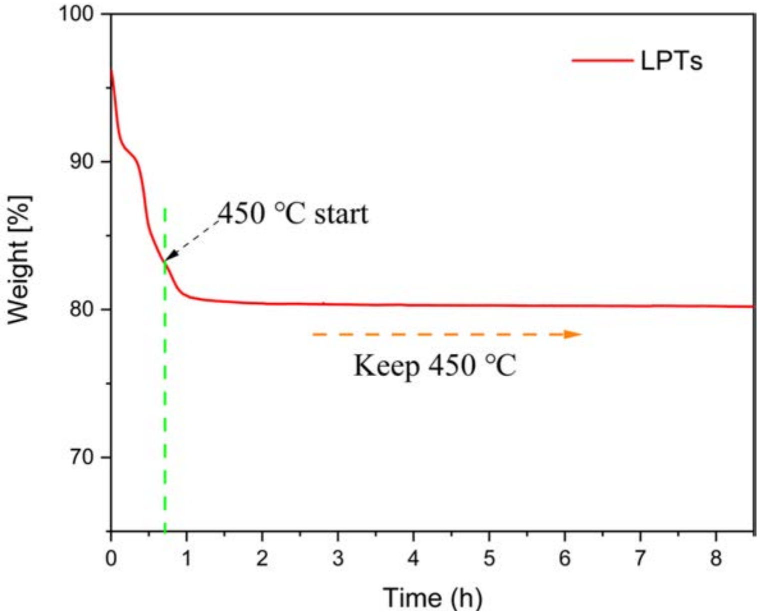

Supplementary Figure 1. Thermal stability of LPTs, evaluated by the TGA.

The calcination condition of LPTs to obtain TiO_2 (450 ^{o}C, 4h) was confirmed to be suitable from the thermal gravimetric analysis (TGA) curve.

In situ XRD

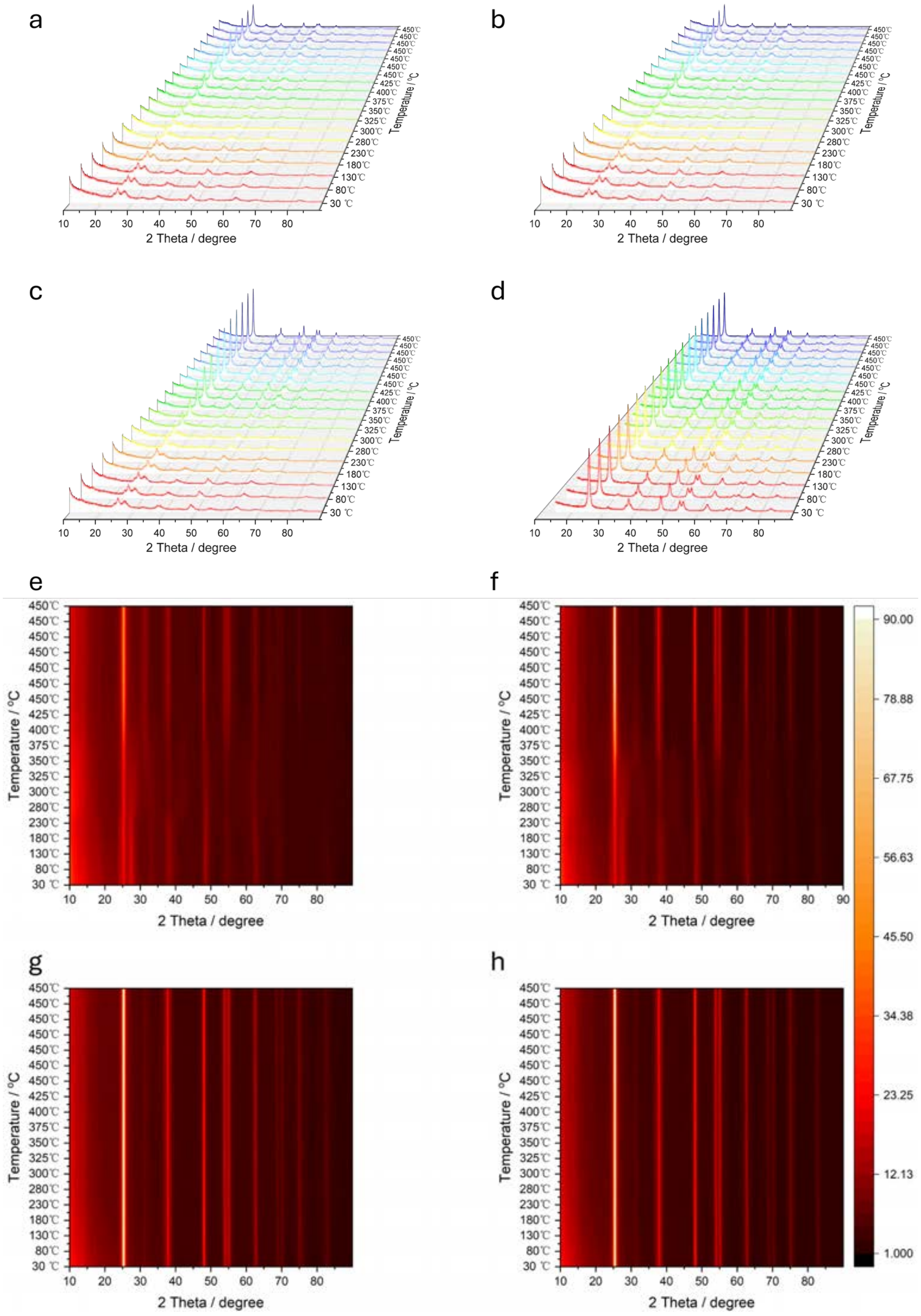

Supplementary Figure 2. *In situ* structural evolution during the synthesis of SS and NP samples, measured by *in situ* XRD technique. (a-h) The *in situ* XRD profiles of 2SS (a), SS support (b), 2NP (c) and NP support (d), along with the corresponding two-dimensional contours plot: 2SS (e), SS support (f), 2NP (g) and NP support (h).

To better understand and compare the phase transformations during sample preparation, *in situ* XRD measurements were performed over 2SS, 2NP, pure SS support and pure NP support. The temperature-dependent *in situ* XRD patterns were collected 5 min after the temperature setpoint was reached. The ramping temperature interval is 50 ºC from the start of 30 ºC with the ramping rate at 1 ºC / min. The transformation from protonated TiO_2 to anatase emerged at 300 ºC and gradually sharpened and finally kept stable at 450 ºC for 2SS. Accordingly, the diffraction peak of protonated TiO_2 disappeared at 300 ºC. As the NP support was obtained from the calcination of LPTs, the peak attributed to TiO_2 for the 2NP sample remained unchanged with the temperature rising from 30 ºC to 450 ºC. Furthermore, no diffraction peak related to Mn salt or Mn nanoclusters was observed for 2SS and 2NP samples due to the trace amount of Mn during *in situ* XRD measurement compared to the pure support, respectively.

Ex situ XRD

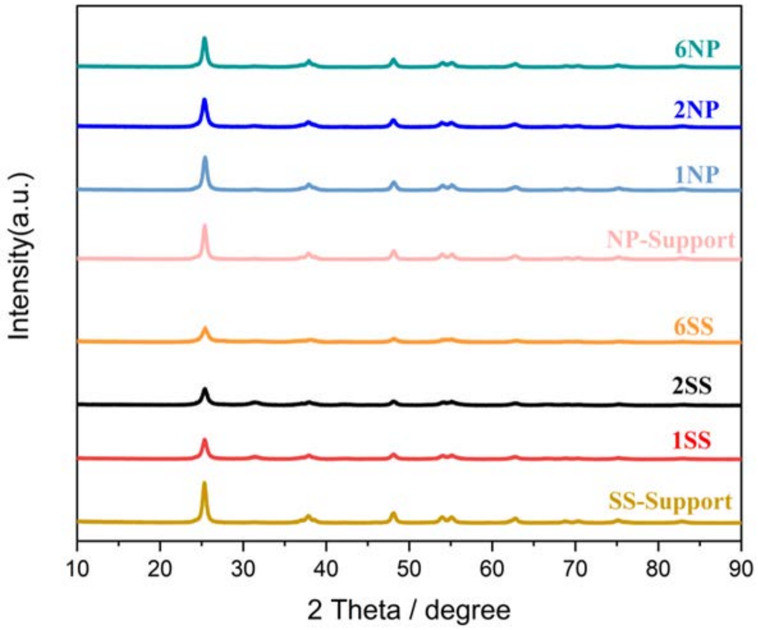

Supplementary Figure 3. *Ex situ* XRD profiles of SS and NP samples and their corresponding supports.

UV-vis and Raman spectra

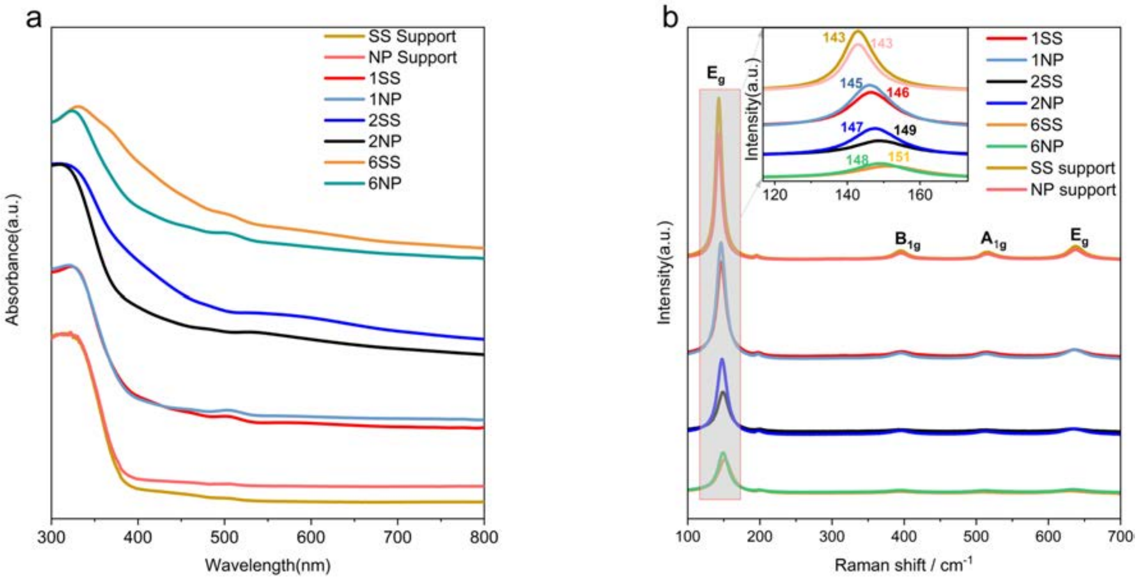

Supplementary Figure 4. Physical structures characterization of SS support, NP support, 1SS, 1NP, 2SS, 2NP, 6SS and 6NP. (a) UV-Vis spectra of SS support, NP support, 1SS, 1NP, 2SS, 2NP, 6SS and 6NP. (b) Raman spectra of SS support, NP support, 1SS, 1NP, 2SS, 2NP, 6SS and 6NP. The inserted graph is the enlarged part at E_g peak.

SEM and TEM

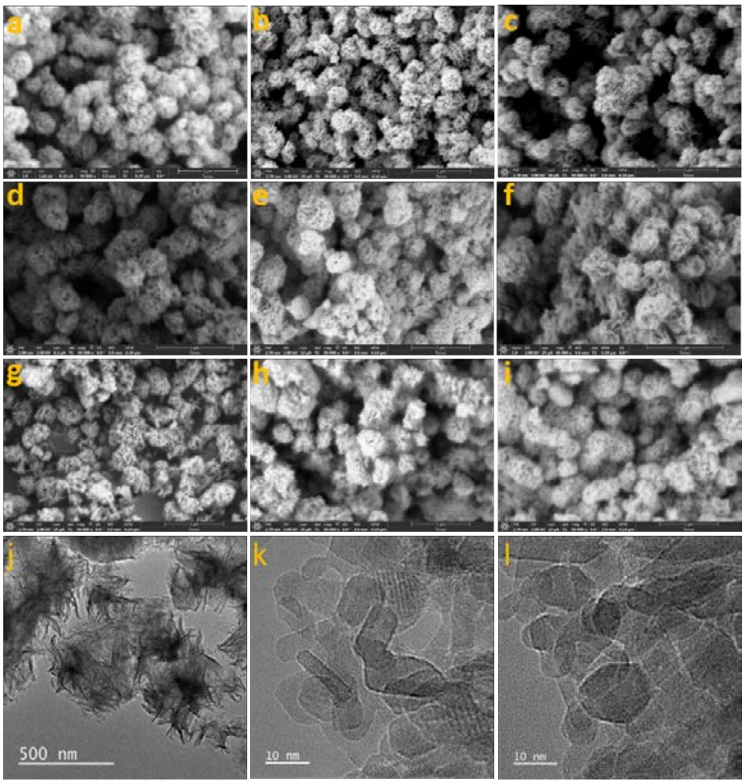

Supplementary Figure 5. Morphology of LPTs, SS support, NP support, SS samples and NP samples. (a-i) The SEM images of LPTS (a), SS support (b), NP support (c), 1SS (d), 1NP (e), 2SS (f), 2NP (g), 6SS (h) and 6NP (i). Scale bar is 1 um. (j-l) Representative TEM images of LPTs (j), 2SS (k) and 2NP (l).

Similar shape and size of sphere were observed over SS and NP samples from SEM images.

N_2 physisorption isotherm

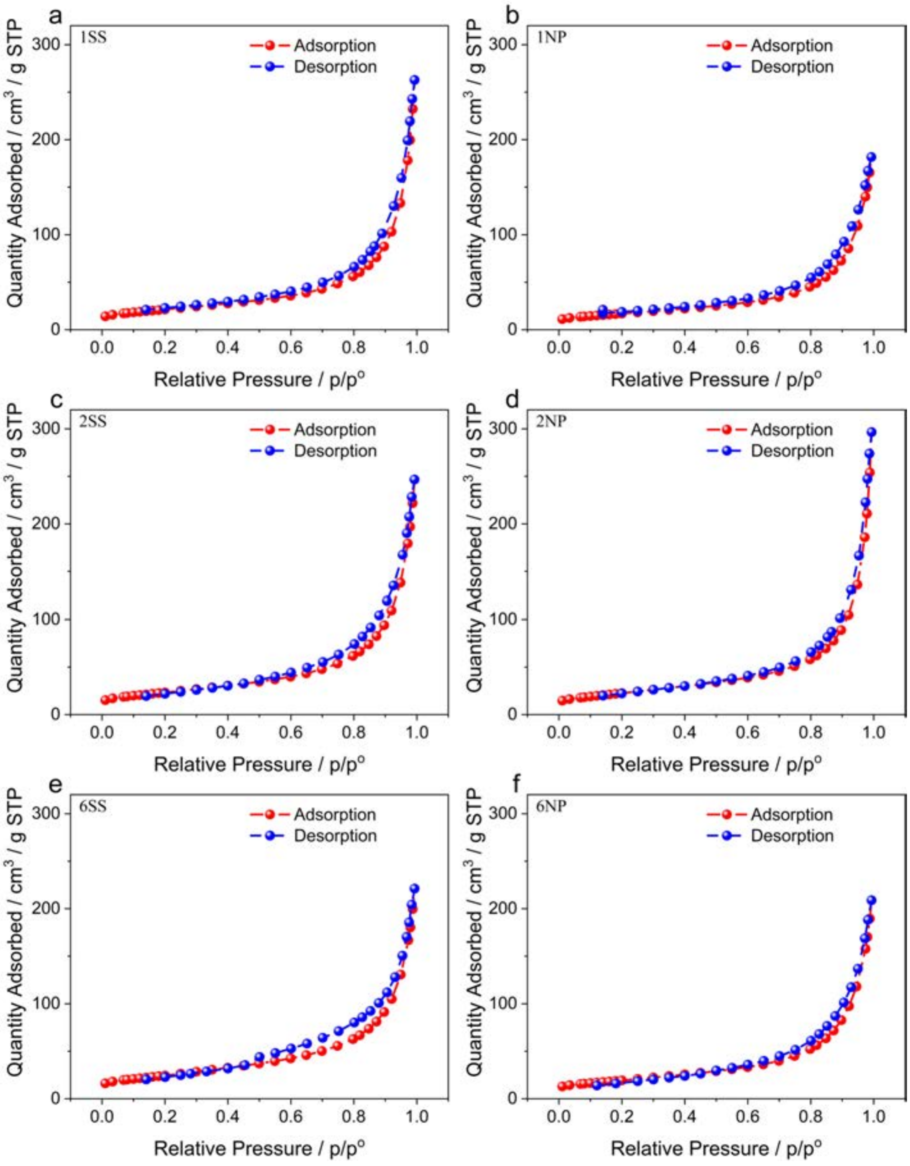

Supplementary Figure 6. Textural properties of SS and NP samples. (a-f) N_2 physisorption isotherm at 77 K of 1SS (a), 1NP (b), 2SS (c), 2NP (d), 6SS (e) and 6NP (f). Corresponding micropore volumes are reported in Supplementary Table 3.

Supplementary Table 3. Physicochemical properties of Mn SS and Mn NP samples.

Sample	**BET surface area / ($m^2 \cdot g^{-1}$)**	**Pore volume / ($cm^3 \cdot g^{-1}$) des**	**Average pore diameter / nm**
1SS	75.9	0.4	19.6
1NP	60.8	0.3	16.7
2SS	83.7	0.4	15.5
2NP	82.1	0.5	19.9
6SS	88.3	0.3	12.4
6NP	69.6	0.3	15.4

Supplementary Note 2. Structure information of SS and NP samples

The structure information of SS and NP samples with various loading (1 wt% ~ 6 wt%) was mainly identified by HAADF-STEM (as discussed in the main text), EXAFS and EPR measurements.

EXAFS analysis revealed no Mn-Mn metallic bonding in the first coordination shell for 1SS, 1NP, 6SS and 6NP samples. The major peak in the first shell was detected for 1SS, 1NP, 6SS and 6NP samples, indicating that the predominant coordination was attributed to Mn-O path in these samples. EXAFS fitting further showed that the coordination number of Mn-O for 1SS, 1NP, 6SS and 6NP samples was 6.0, 5.9, 4.4 and 4.0, the Mn-O bond length for 1SS, 1NP, 6SS and 6NP samples was 2.07 Å, 2.13 Å, 1.86 Å and 1.82 Å in the first shell (**Supplementary Fig. 12** and **Supplementary Table 4**). Additionally, wavelet transform (WT) EXAFS analysis was also performed conducted to distinguish the second-shell coordination environments (**Supplementary Fig. 13**)[3]. However, due to the very low contrast in backscattering amplitudes between Mn and Ti[4], it remains challenging to clearly identify contributions from Mn-O-Ti or Mn-O-Mn coordination in the second shell for SS and NP samples with different Mn loadings using WT EXAFS.

Consistent with the EPR results of 2SS and 2NP samples, hyperfine split lines signals attributed to the isolated Mn^{2+} species were also detected in 1SS and 6SS samples (**Supplementary Fig. 14**). In contrast, the 1NP and 6NP samples exhibited a broad signal in the 3000 ~ 3600 G range, which was the characteristic of ferromagnetic resonance from Mn^{2+} species. This broad feature indicates the presence of large amount of MnO_x aggregates or clusters in 1NP and 6NP samples[5]. Additionally, the 1NP, 2NP, and 6NP samples exhibited a hole-related signal at g value of 2.005, identical to that observed in the SS and NP supports composed of pure TiO_2. This signal was attributed to radical $Ti^{4+}O^{2-}Ti^{4+}O^{\bullet-}$ from TiO_2 and it was not detected in 1SS, 2SS and 6SS samples[6], indicating that radical $Ti^{4+}O^{2-}Ti^{4+}O^{\bullet-}$ was replaced by Mn atoms in SS samples, further verifying the existence of greater lattic distortion between Mn species and TiO_2 in SS samples compared to NP samples[7,8]. In summary, these combined results from STEM-EDX/EELS, EXAFS and EPR confirmed that 1SS and 6SS samples have similar Mn structures as 2SS sample, while 1NP and 6NP samples exhibit similar Mn structures as 2NP sample.

STEM-EDX

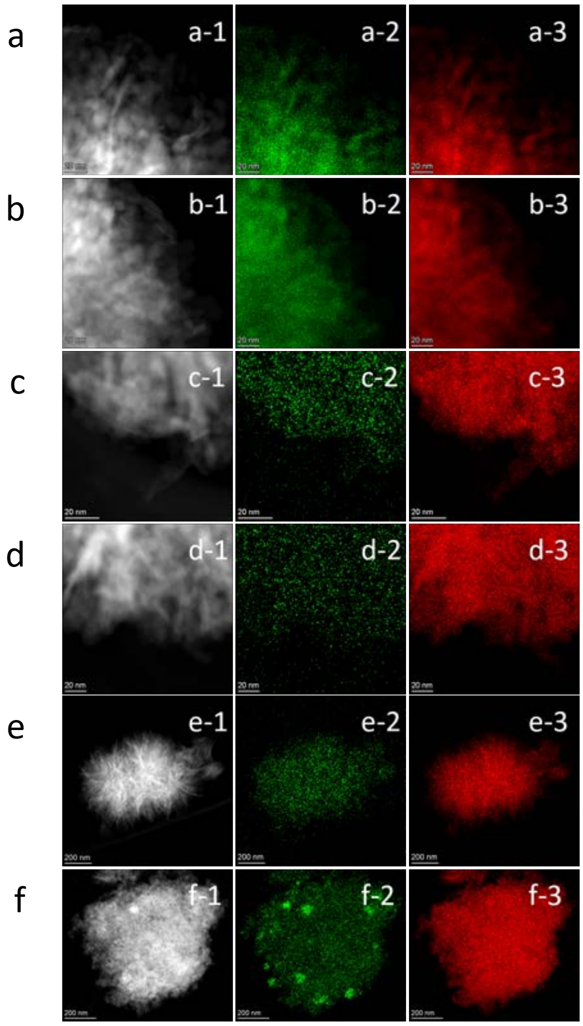

Supplementary Figure 7. AC-HAADF-STEM and EDX mapping of SS and NP samples. (a-f) STEM images and corresponding EDX elemental maps of 1SS (a), 1NP (b), 2SS (c), 2NP (d), 6SS (e), 6NP (f). Green represents Mn, red represents Ti.

STEM-EELS

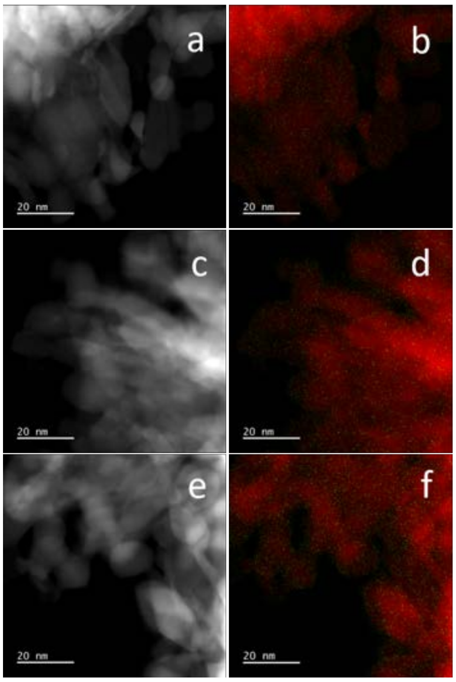

Supplementary Figure 8. AC-HAADF-STEM and EELS mapping of 1SS in different regions. (a-f) STEM images (a, c and e) and corresponding EELS elemental maps of 1SS (b, d and f). Green represents Mn, red represents Ti.

For the 1SS sample, no obvious MnO_x nanoclusters were detected in different regions from HAADF-STEM-EELS images.

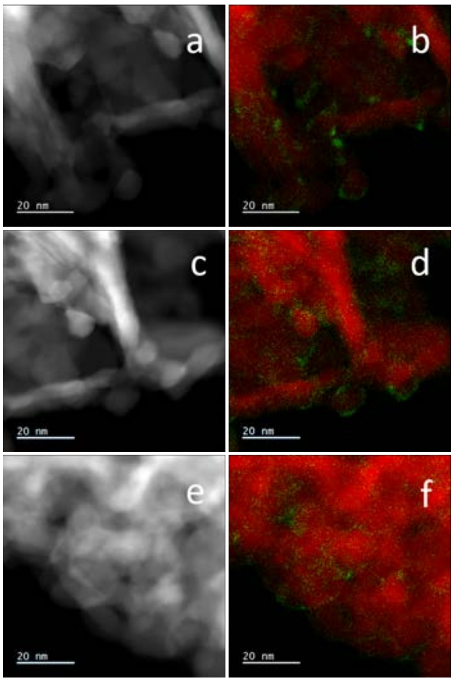

Supplementary Figure 9. AC-HAADF-STEM and EELS mapping of 2NP in different regions. (a-f) STEM images (a, c and e) and corresponding EELS elemental maps of 2NP (b, d and f). Green represents Mn, red represents Ti.

For 2NP sample, various MnO_x nanoclusters were found in different regions from HAADF-STEM-EELS images, thus confirming that the majority of Mn species exist as MnO_x nanoclusters in this sample.

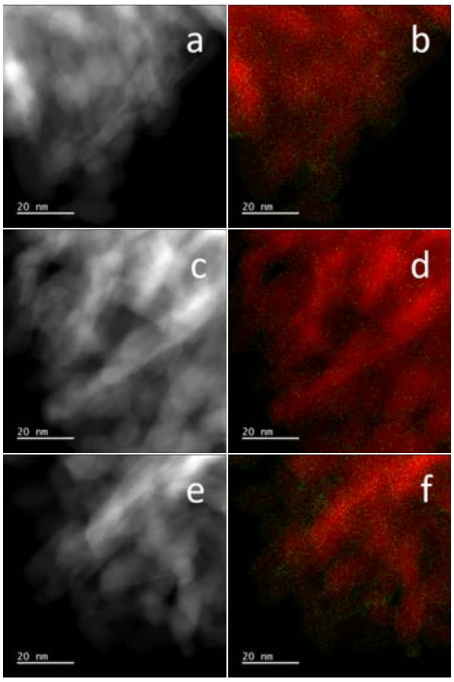

Supplementary Figure 10. AC-HAADF-STEM and EELS mapping of 1NP in different regions. (a-f) STEM images (a, c and e) and corresponding EELS elemental maps of 1NP (b, d and f). Green represents Mn, red represents Ti.

In the 1NP sample, MnO_x nanoclusters are clearly observed particularly in Supplementary Fig. 10f, further confirming higher concentration of MnO_x nanoclusters in 1NP compared to 1SS.

EXAFS

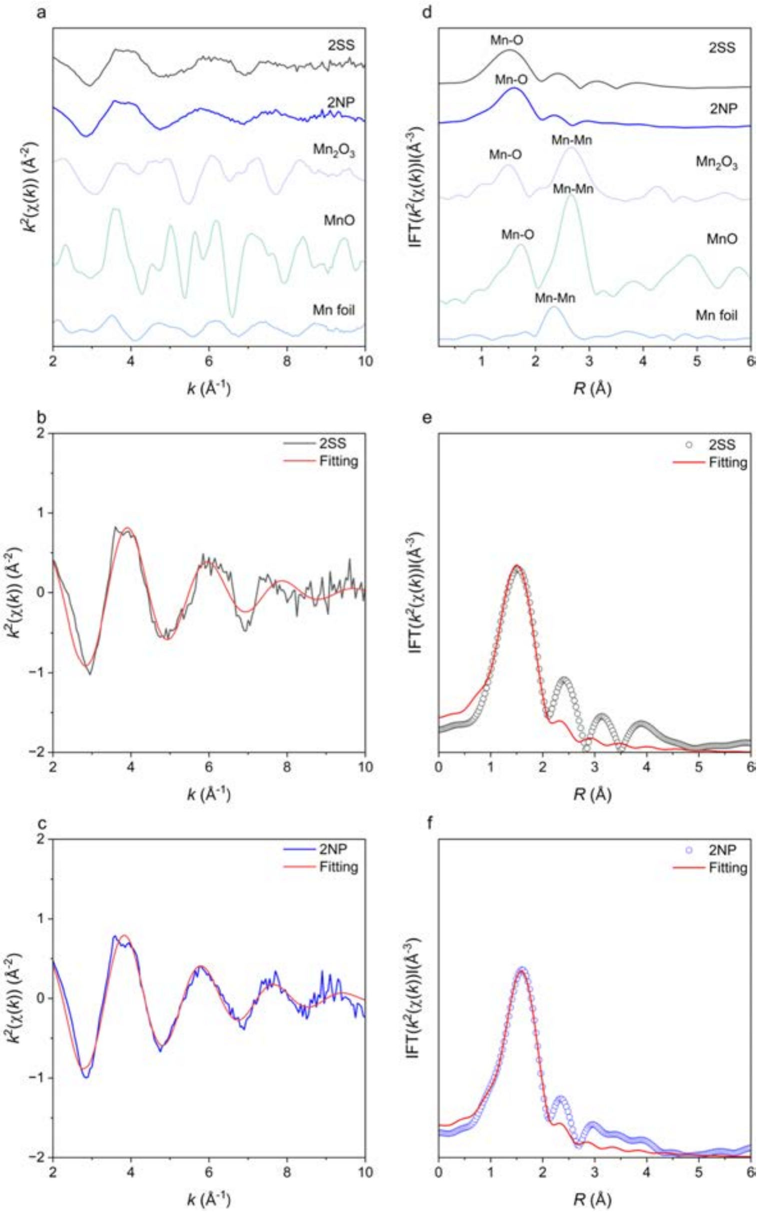

Supplementary Figure 11. k^2-weighted EXAFS oscillations and corresponding Fourier-transformed EXAFS spectra at the Mn K-edge for 2SS and 2NP samples, compared to Mn foil, Mn_2O_3 and MnO references. (a) EXAFS spectra of 2SS and 2NP samples in k space, compared to Mn foil, Mn_2O_3 and MnO references. (b-c) EXAFS fitting in k space for 2SS (b) and 2NP (c). (d) EXAFS spectra in R space for 2SS and 2NP samples compared with Mn foil, Mn_2O_3 and MnO references. (e-f) EXAFS fitting in R space for 2SS (e) and 2NP (f).

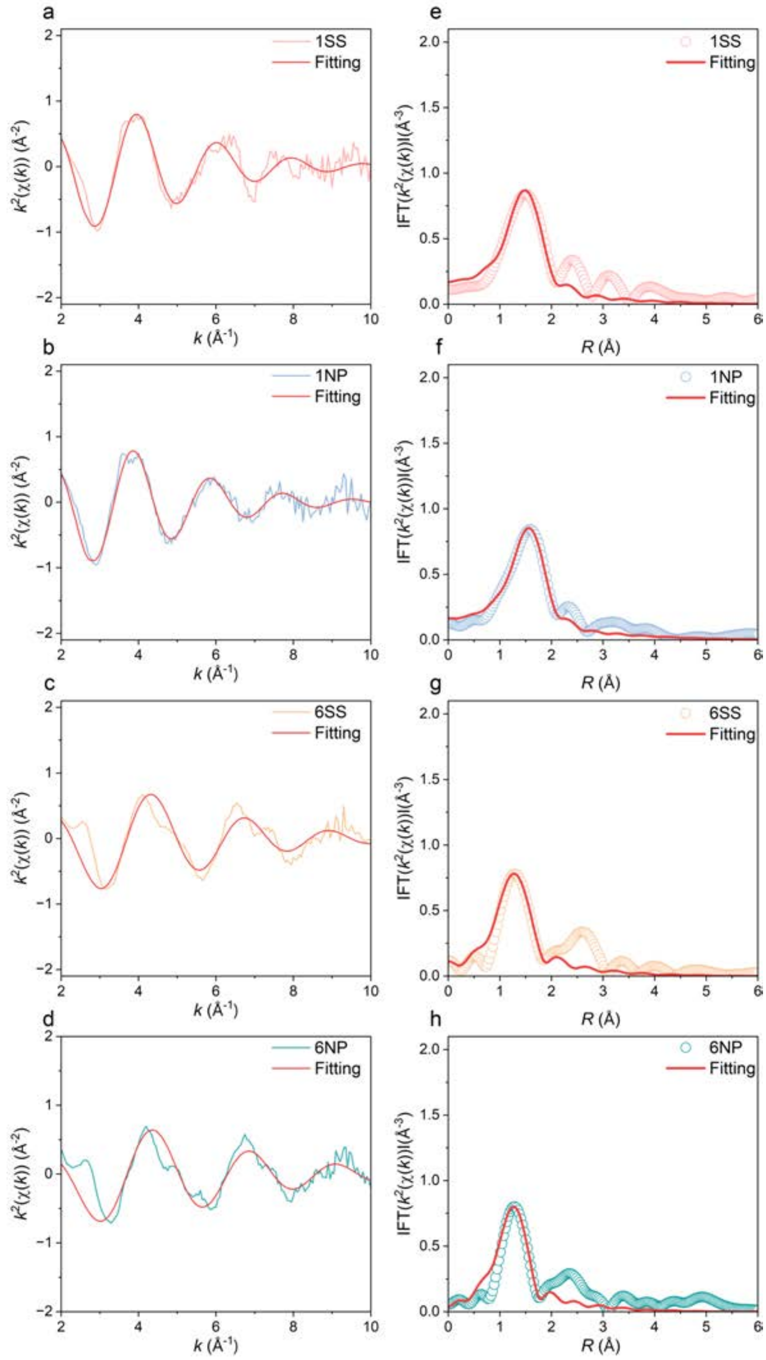

Supplementary Figure 12. k^2-weighted EXAFS spectra at the Mn K-edge of 1SS, 1NP, 6SS and 6NP. (a-d) EXAFS spectra in k space for 1SS (a), 1NP (b), 6SS (c), and 6NP (d). (e-h) Corresponding EXAFS fitting spectra in R space for 1SS (e), 1NP (f), 6SS (g), and 6NP (h).

Supplementary Table 4. EXAFS fitting parameters at Mn K-edge for Mn SS samples, Mn NP samples and MnO.

Sample	Shell	CN[a]	R[b] [Å]	σ^2 [c] [Å^2]	R[d]-factor [%]
MnO	Mn-O	6*	2.20 ± 0.01	0.008 ± 0.002	0.7
1SS	Mn-O	6.0 ± 1.0	2.07 ± 0.01	0.014 ± 0.003	0.7
1NP	Mn-O	5.9 ± 1.0	2.13 ± 0.02	0.015 ± 0.003	0.6
2SS	Mn-O	6.0 ± 1.0	2.09 ± 0.01	0.014 ± 0.003	0.6
2NP	Mn-O	5.5 ± 1.0	2.14 ± 0.02	0.012 ± 0.003	1.0
6SS	Mn-O	4.4 ± 0.4	1.86 ± 0.08	0.010 ± 0.005	0.4
6NP	Mn-O	4.0 ± 0.5	1.82 ± 0.02	0.008 ± 0.003	1.8

a) CN: Coordination numbers; b) R: Bond distance; c) σ^2: Debye-Waller factors; d) R factor: The values of R factor quantify the goodness of fit when fitting all data scans for each sample. S_0^2 was fixed to 0.789 according to the experimental EXAFS fitting of MnO by fixing CN as the known crystallographic value. * This value was fixed during EXAFS fitting, based on the known structure of MnO. The fitting range of k space for relevant references and samples were as follows, MnO: 2.44 ~ 11.00 Å^{-1}. Mn_2O_3: 2.54 ~ 11.09 Å^{-1}. MnO_2: 3.03 ~ 13.01 Å^{-1}. 1SS: 2.34 ~ 8.15 Å^{-1}. 1NP: 2.29 ~ 8.84 Å^{-1}. 2SS: 2.35 ~ 8.03 Å^{-1}. 2NP: 2.32 ~ 8.70 Å^{-1}. 6SS: 2.79 ~ 8.51 Å^{-1}. 6NP: 2.85 ~ 9.56 Å^{-1}.

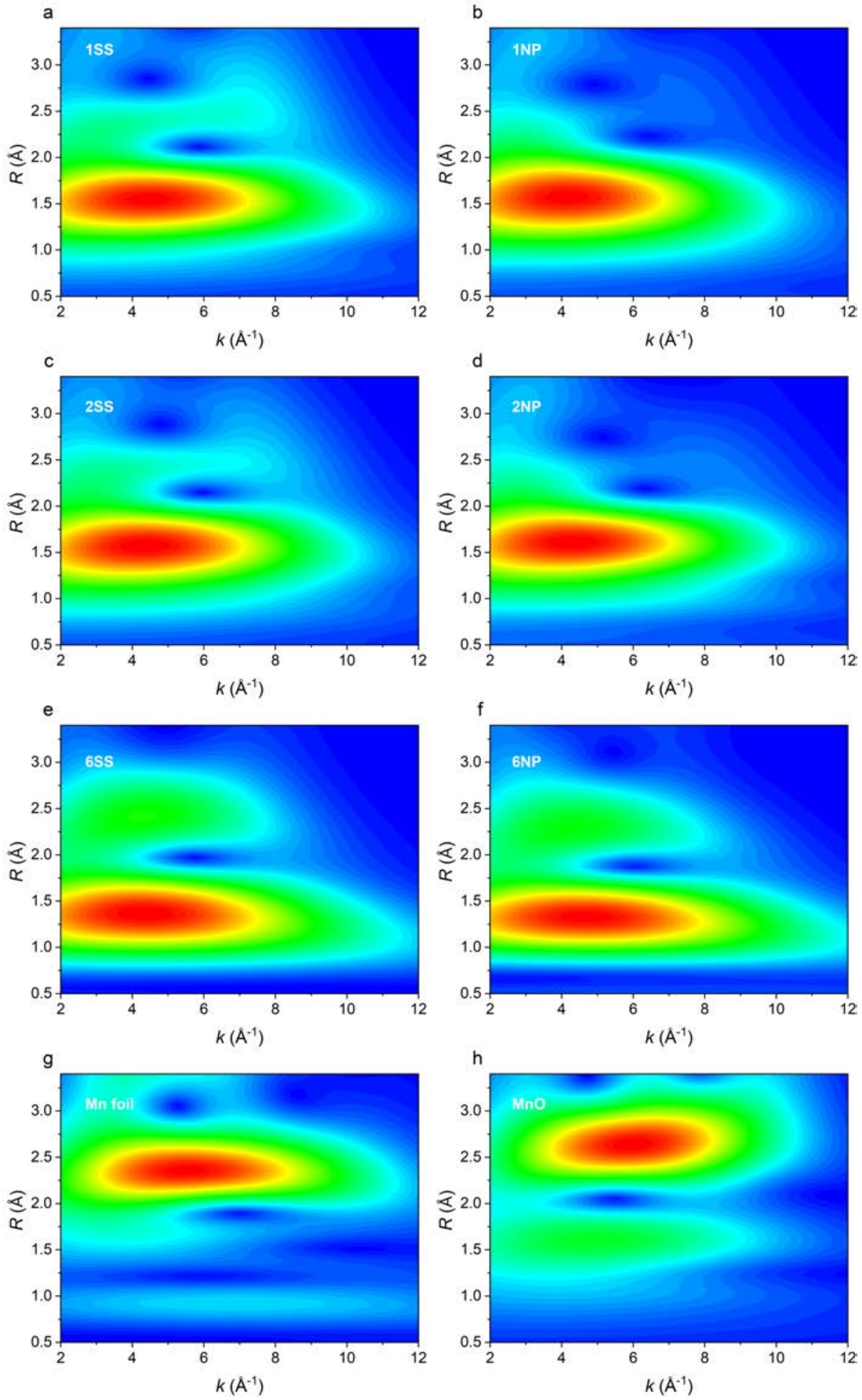

Supplementary Figure 13. Wavelet transform for k^2-weighted EXAFS signals at the Mn K-edge for Mn samples: (a) 1SS, (b) 1NP, (c) 2SS, (d) 2NP, (e) 6SS, (f) 6NP, (g) Mn foil, and (h) MnO.

EPR

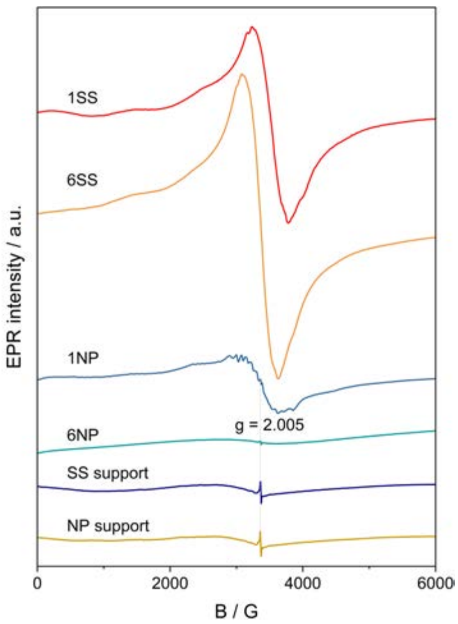

Supplementary Figure 14. EPR spectra of 1SS, 1NP, 6SS, 6NP samples, SS support and NP support.

Supplementary Note 3. Mn oxidation state and redox property.

The oxidation state of Mn species in SS and NP samples was mainly evaluated by XANES, XPS measurements. XANES analysis revealed that the absorption edges of both 2SS and 2NP fall between those of MnO and Mn_2O_3 (**Supplementary Fig. 15a**), indicating bulk Mn oxidation state between 2 and 3. 2SS samples have slightly higher Mn oxidation state (~ 2.5) than 2NP samples (~ 2.4), calculated from the first derivative of XANES (**Supplementary Figs. 15b, 16a**). Similarly, for the 1SS, 1NP, 6SS and 6NP samples (**Supplementary Figs. 16b, c**), the absorption edges of 1SS and 6SS in the XANES spectra slightly shifted toward higher energy compared to those of 1NP and 6NP, respectively, suggesting subtly higher Mn oxidation states in the SS samples. The corresponding Mn oxidation states were estimated to be ~ 2.5 for 1SS, ~ 2.6 for 6SS, ~ 2.4 for 1NP, and ~ 2.5 for 6NP.

To gain further insight into the surface oxidation states, high-resolution XPS analysis of Mn 2p, Mn 3s, Ti 2p, and O 1s were performed (**Supplementary Figs. 15c-e, Supplementary Figs. 17-18 and Supplementary Tab 5**). The Mn 2p peak fitting followed the method from our previous work[9], which involved referencing the spectra of standard MnO, Mn_2O_3, and MnO_2. These references were used to deconvolute the Mn $2p_{3/2}$ spectra of the samples and calculate the average oxidation states. The 2SS sample exhibited a slightly higher surface Mn oxidation state (~ 2.8) than the 2NP sample (~ 2.7). Additionally, the Mn 3s spectra provided further insight into the Mn oxidation state. The binding energy difference between the two multiplet-split components arises from the interaction between the non-ionized 3s electron and 3d valence electrons[10]. The Mn average oxidation states of 2SS and 2NP were found to be between 2 and 3 from the Mn 3s spectra (**Supplementary Fig. 15e)**, as their magnitude of peak splitting are located in the range from 5.3 eV to 6.0 eV, which is the characteristic of Mn_2O_3 and MnO, respectively[10]. The same analysis applied to the 1SS, 1NP, 6SS and 6NP samples showed surface Mn oxidation states of 2.6, 2.4, 2.6 and 2.4, respectively (**Supplementary Fig. 19** and **Supplementary Tab 5**). Consistently, their

Mn 3s spectra also showed peak splitting in the range from 5.3 eV to 6.0 eV (**Supplementary Fig. 20**), indicating average Mn oxidation state of these samples between 2 and 3. In summary, combining the XANES and XPS results (**Supplementary Tab 6)**, we conclude that all SS and NP samples possess average Mn oxidation state close to 2.5, with only subtle differences between them.

In general, the redox property plays a crucial role in determining the catalytic performances for NH_3-SCR reaction. To evaluate the redox behavior, NO oxidation tests were conducted on both SS and NP samples (**Supplementary Fig. 15f** and **Supplementary Fig. 21**). The 2NP sample exhibited higher NO conversion than the 2SS sample, which behavior discrepancy was different from that of Mn valence of these samples, indicating other factors must be related to this performance. Besides, no N_2O formation was detected during NO oxidation. Similarly, 1NP and 6NP samples showed consistently higher NO conversion comparted to 1SS and 6SS samples from 150 ^{o}C to 400 ^{o}C, respectively. These results further confirm that the NP samples have stronger oxidation function than SS samples.

Mn oxidation state

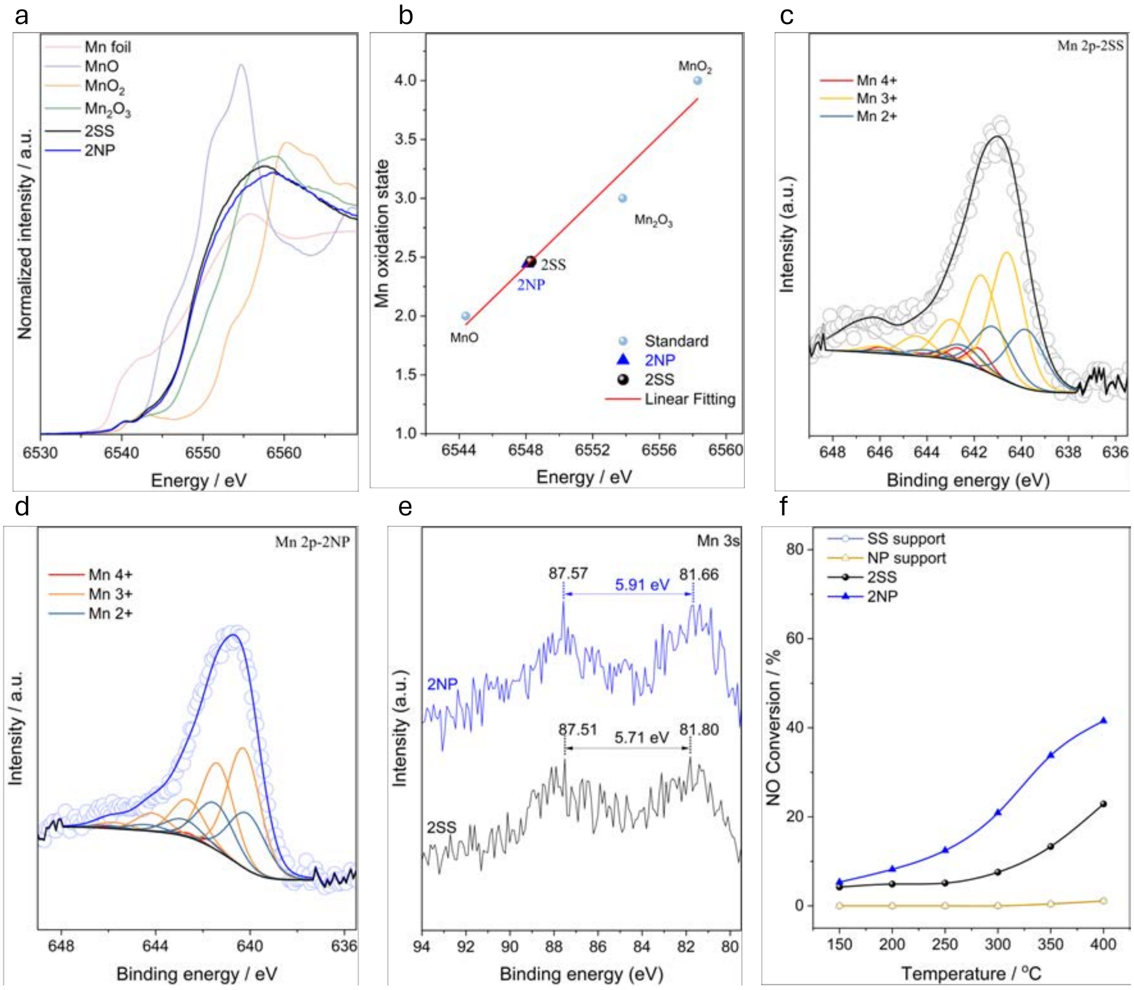

Supplementary Figure 15. Mn oxidation states and redox properties. (a) Mn K-edge XANES spectra of 2SS, 2NP compared with Mn foil, MnO, MnO_2 and Mn_2O_3 references. (b) Mn oxidation states of 2SS and 2NP. (c-d) the Mn 2p XPS spectra of 2SS (c) and 2NP (d). (e) the Mn 3s XPS spectra of 2SS and 2NP. (f) NO oxidation catalytic performance for 2SS, 2NP and their supports. Reaction conditions for NO oxidation: 0.075 g catalyst, 0.1 Mpa, 150-400 °C, 5 % O_2, 450 ppm NO, 333 ml /min total flow rate, 40000 h^{-1} GHSV.

XANES

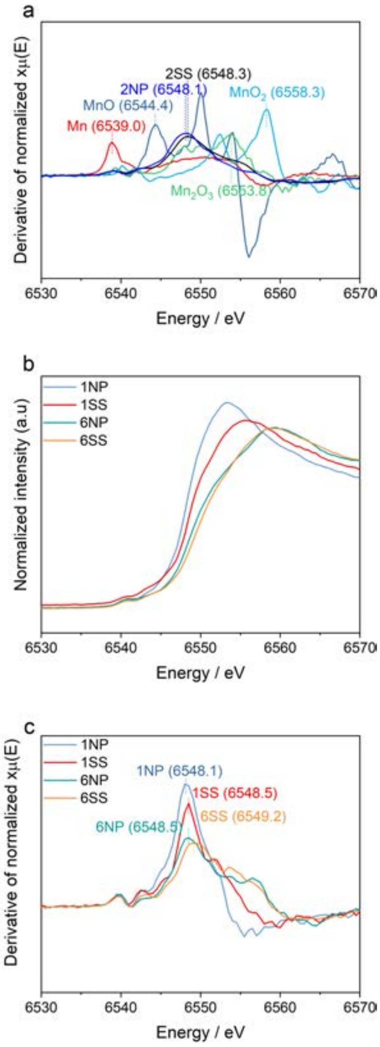

Supplementary Figure 16. XANES spectra of SS samples, NP samples and Mn references (Mn foil, MnO, Mn_2O_3 and MnO_2). (a) Derivative of normalized XANES spectra for 2SS, 2NP, Mn foil, MnO, Mn_2O_3 and MnO_2. (b) Normalized XANES of 1SS, 1NP, 6SS and 6NP. (c) Derivative of normalized XANES spectra for 1SS, 1NP, 6SS and 6NP.

XPS

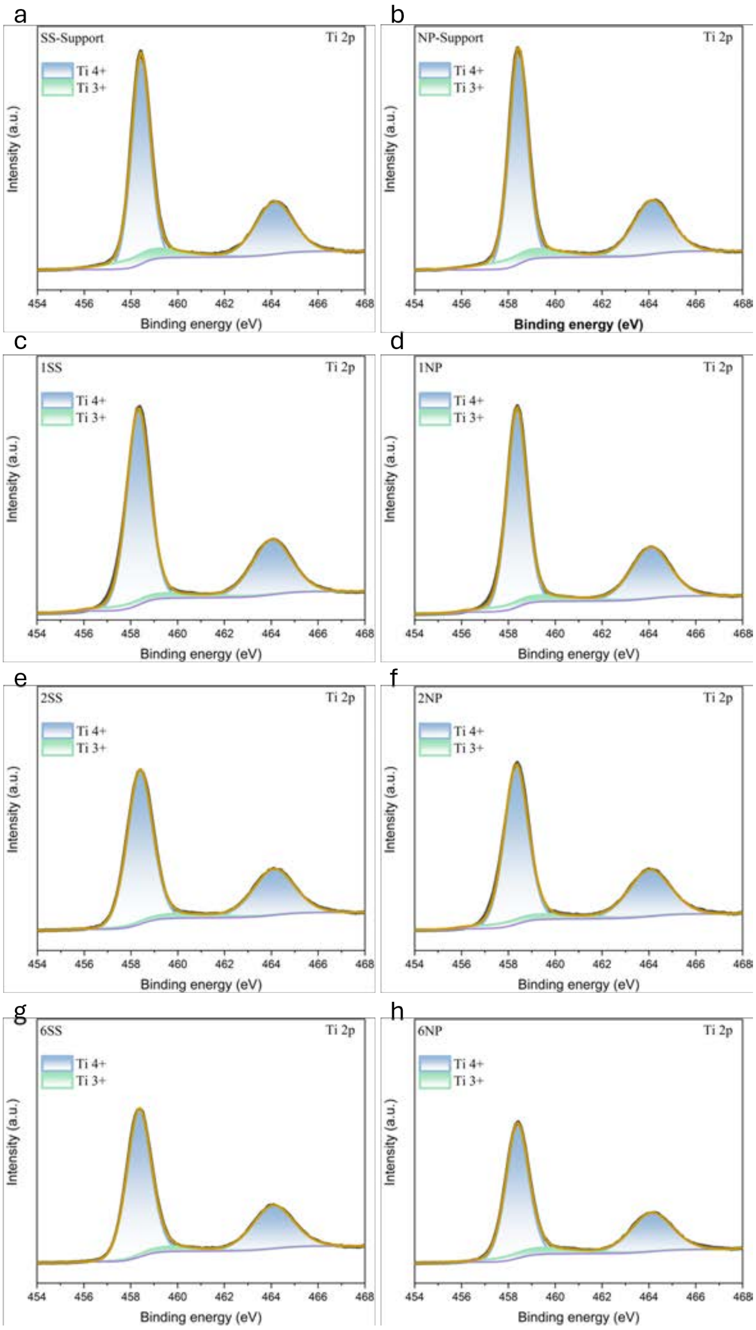

Supplementary Figure 17. Surface valence analysis of Ti element in SS support, NP support, SS and NP samples. (a-h) the Ti 2p spectrum of XPS in SS support (a), NP support (b), 1SS (c), 1NP (d), 2SS (e), 2NP (f), 6SS (g) and 6NP (h).

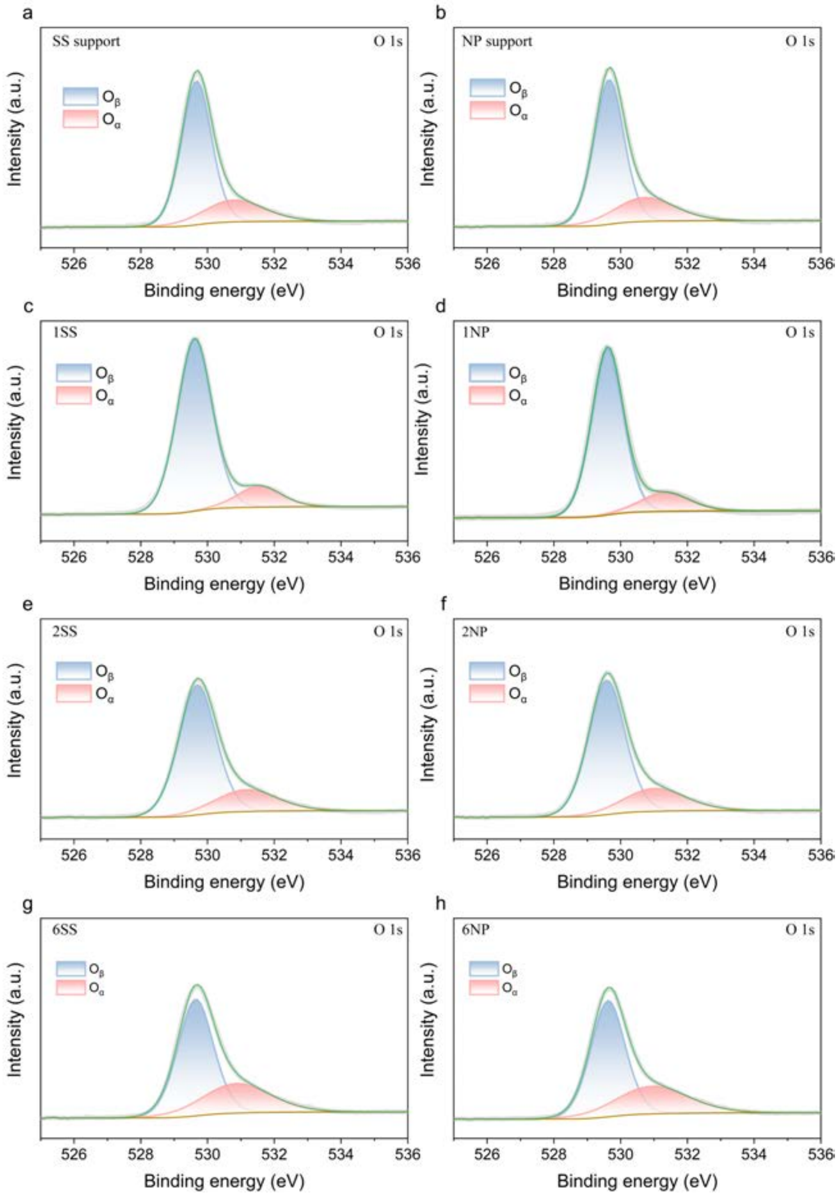

Supplementary Figure 18. Surface valence analysis of O element in SS support, NP support, SS and NP samples. (a-h) the O 1s spectrum of XPS in SS support (a), NP support (b), 1SS (c), 1NP (d), 2SS (e), 2NP (f), 6SS (g) and 6NP (h).

O_α: adsorbed oxygen on the catalyst surface.

O_β: lattice oxygen in the catalyst[11].

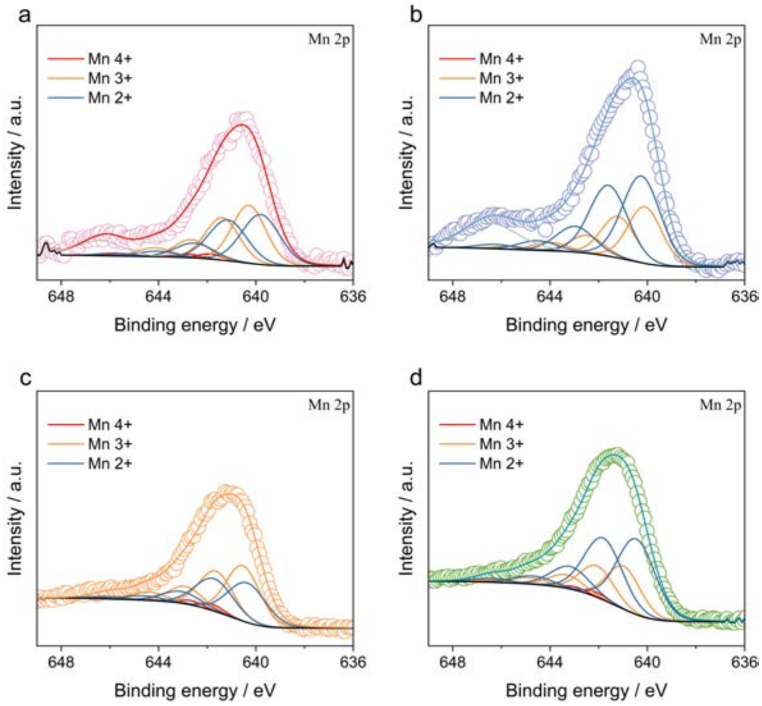

Supplementary Figure 19. Surface valence analysis of Mn element in 1SS, 1NP, 6SS and 6NP samples. (a-d) the Mn 2p spectra of XPS in 1SS (a), 1NP (b), 6SS (c) and 6NP (d) samples.

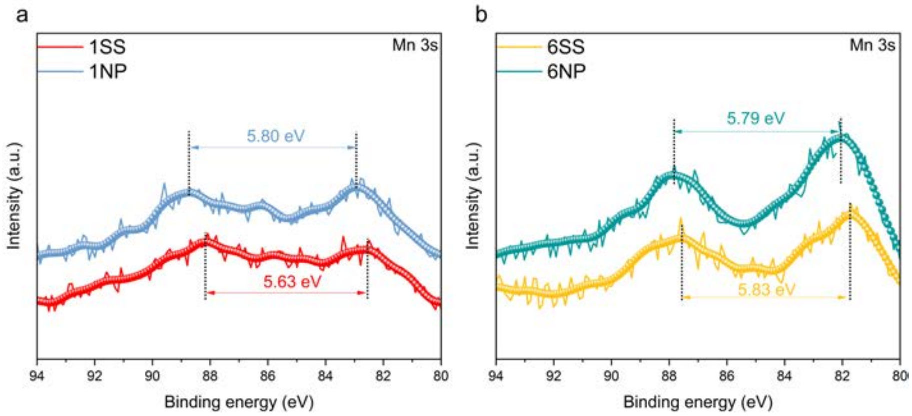

Supplementary Figure 20. The additional surface valence analysis of Mn element from Mn 3s XPS spectra in 1SS, 1NP, 6SS and 6NP samples. (a) the Mn 3s XPS spectra of 1SS and 1NP. (b) the Mn 3s XPS spectra of 6SS and 6NP.

Supplementary Table 5. Quantitative XPS analysis of Mn 2p, Ti 2p, and O 1s spectra for Mn SS samples, Mn NP samples, SS support and NP support.

Sample	**Ti**		**O**		**Mn**		
	Ti^{4+} / %	Ti^{3+} / %	O_α / %	O_β / %	Mn^{4+} / %	Mn^{3+} / %	Mn^{2+} / %
1SS	93.03	6.97	13.40	86.60	3.27	48.75	47.98
1NP	91.99	8.01	14.69	85.31	0.24	36.34	63.42
2SS	94.65	5.35	21.81	78.19	7.22	60.94	31.84
2NP	92.42	7.58	22.46	77.54	2.35	63.40	34.25
6SS	95.26	4.74	32.73	67.27	4.57	52.58	42.85
6NP	90.88	9.12	33.25	66.75	2.73	32.34	64.93
SS support	89.29	10.71	23.39	76.61	-	-	-
NP support	89.25	10.75	25.17	74.83	-	-	-

Supplementary Table 6. Average Mn oxidation state determined from XANES and XPS analysis.

Sample	Average Mn valence from XANES	Average Mn valence from XPS
1SS	2.5	2.6
1NP	2.4	2.4
2SS	2.5	2.8
2NP	2.4	2.7
6SS	2.6	2.6
6NP	2.5	2.4

NO oxidation reaction

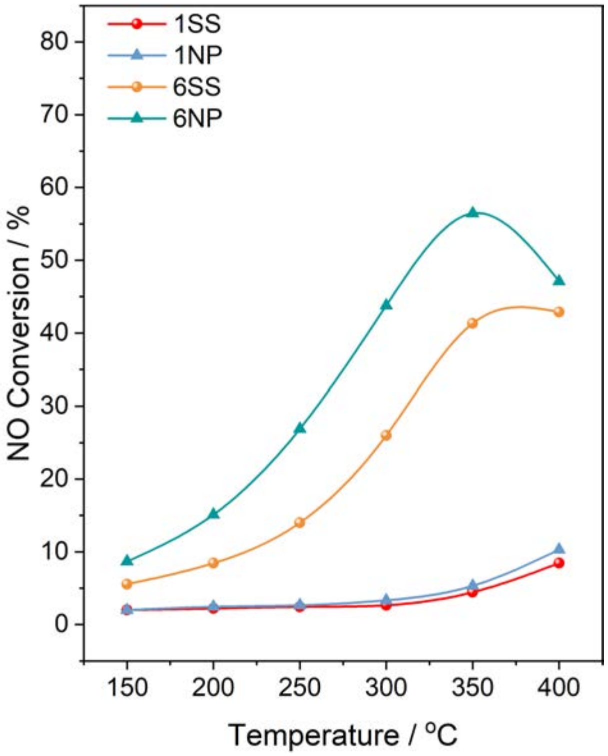

Supplementary Figure 21. NO oxidation catalytic performance of 1SS, 1NP, 6SS and 6NP samples. Reaction conditions for NO oxidation: 0.075g catalyst, 0.1 Mpa, 150-400 °C, 5 % O_2, 450 ppm NO, 333ml /min total flow rate, 40000 h^{-1} GHSV.

Supplementary Note 4. Acidity of SS and NP samples.

Furthermore, to investigate the redox properties and acidity of the SS and NP samples, we conducted temperature-programmed desorption experiments of NO (NO-TPD) and NH_3 (NH_3-TPD) (**Supplementary Figs. 22-23**). The amount of desorbed NO, NH_3 and N_2O were calculated accordingly (**Supplementary Tables 7** and **8**).

For the NO-TPD experiment (**Supplementary Fig. 22**), two desorption peaks appeared at the range of 100 ~ 125 °C and above 125 °C. The similar amount of desorbed NO was observed from 100 °C to 125 °C in both 2SS and 2NP sample, which were attributed to the physically adsorbed NO molecule, consistent with control experiments on the pure SS and NP supports. More NO chemical desorption amount was detected in 2NP (0.005 mmol / g) compared to 2SS (0.002 mmol / g) above 125 °C, indicating enhanced NO interaction with the Mn nanoclusters. Notably, the temperature of the N_2O formation peak during NO desorption was lower in 2NP sample (~ 305 °C) compared to 2SS (~ 350 °C), suggesting that N_2O species form more readily on the Mn nanocluster with close Mn proximity, thus obviously confirmed different redox functions existed in 2SS and 2NP samples. Similar trends were observed for the 1 wt% and 6 wt% sample: 1NP and 6NP exhibited NO desorption amounts of 0.002 mmol / g and 0.012 mmol / g, respectively, whereas 1SS and 6SS showed lower values of 0.001 mmol / g and 0.002 mmol / g. Correspondingly, the N_2O formation peaks appeared at lower temperatures for the NP samples (~ 343 °C for 1NP and ~ 271 °C for 6NP) compared to the SS samples (~ 386 °C for 1SS and ~ 301 °C for 6SS). These results indicated that Mn nanoclusters in the NP samples facilitate N_2O formation during the NO desorption process, providing further evidence of their distinct redox behavior compared to isolated Mn sites in the SS samples. Notably, no N_2O formation was detected from either the SS or NP supports alone, confirming that Mn species are essential for N_2O generation under these conditions.

For the NH_3-TPD experiment (**Supplementary Fig. 23**), more amounts of desorbed NH_3 were produced in 2SS sample (0.259 mmol / g) compared to 2NP sample (0.148 mmol / g) after dosing same amount of NH_3 over them, indicating stronger surface acidity in 2SS despite their comparable Mn oxidation states. Furthermore, the formation of N_2O during the desorption process provides indication on the catalyst redox function. In all cases, the 2NP sample produced more N_2O (0.026 mmol / g) at lower temperatures (~ 290 °C and ~ 170 °C) compared to the 2SS (0.020 mmol / g, ~ 327 °C), which suggest that the redox function of 2NP is much stronger. Similarly, for 1SS, 1NP, 6SS and 6NP samples, more amounts of desorbed NH_3 were produced in 1SS (0.311 mmol / g) and 6SS samples (0.148 mmol / g) than 1NP (0.156 mmol / g) and 6NP samples (0.119 mmol / g), confirming higher acidity in the SS samples. Conversely, the 1NP and 6NP samples produced more N_2O (0.020 mmol / g for 1NP, 0.037 mmol / g for 6NP) at lower temperatures (~ 165 °C and ~ 292 °C for 1NP, ~ 169 °C and ~ 280 °C for 6NP) compared to 1SS and 6SS samples (0.007 mmol / g at ~ 369 °C for 1SS, 0.024 mmol / g at ~ 316 °C for 6SS). These results clearly demonstrate the stronger redox behavior of NP samples compared to SS samples. Additionally, no N_2O formation was detected from the SS support and NP support alone during NH_3-TPD, confirming that N_2O generation is directly related to the presence of Mn species in the samples.

NO-TPD

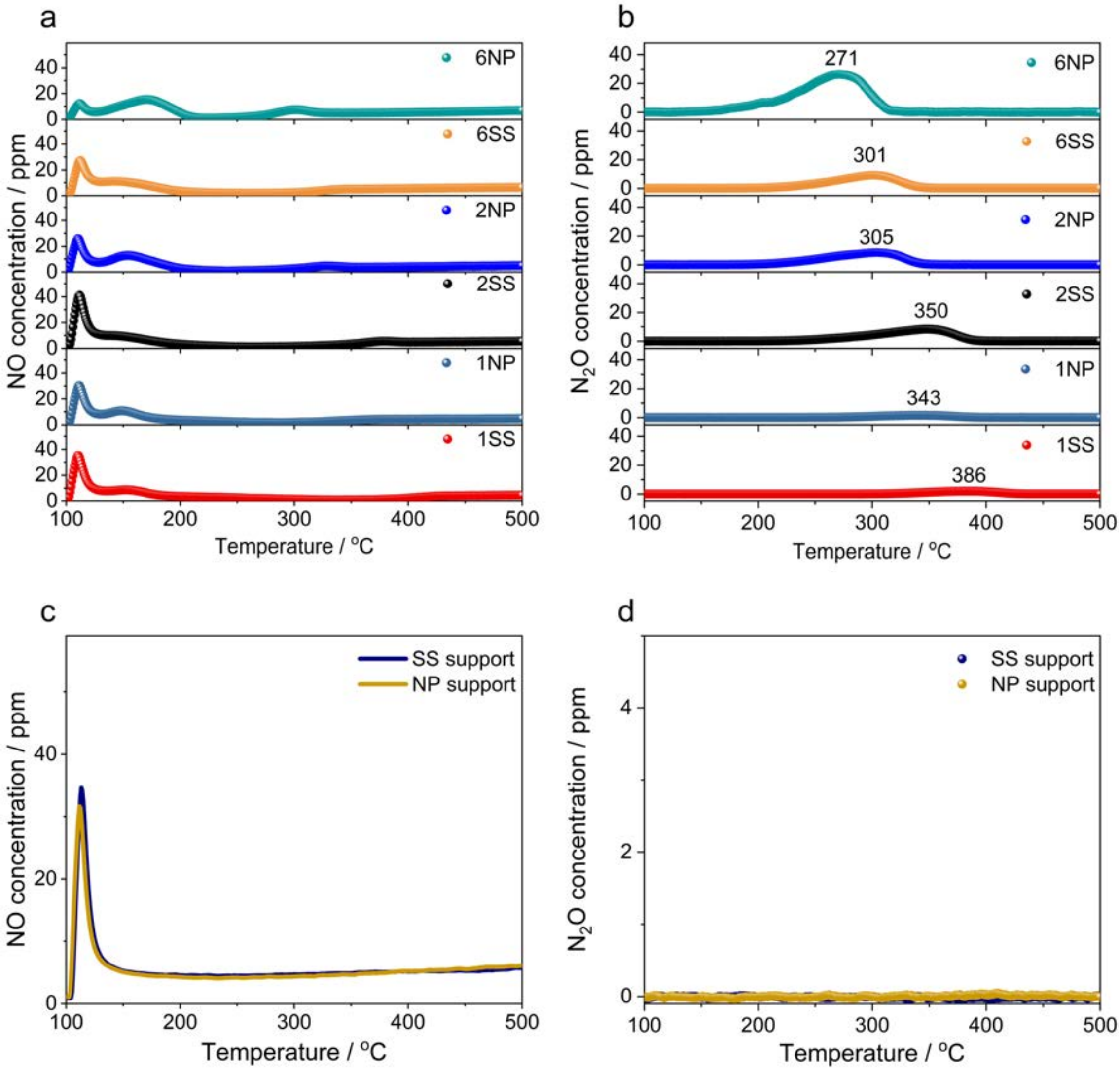

Supplementary Figure 22. Interaction between NO probe molecules and active sites evaluated by NO-TPD. (a) NO desorption profiles as a function of temperature for 1SS, 1NP, 2SS, 2NP, 6SS and 6NP. (b) N_2O formation during NO desorption for 1SS, 1NP, 2SS, 2NP, 6SS and 6NP. (c) NO desorption profiles for SS support and NP support. (d) N_2O desorption profiles for SS support and NP support.

Supplementary Table 7. Chemical desorption (temperature above 125 ^{o}C) amount of NO and N_2O during NO-TPD measurement.

Sample	NO desorption amount / mmol / g	N_2O formation amount mmol / g
1SS	0.001	0.001
1NP	0.002	0.002
2SS	0.002	0.011
2NP	0.005	0.012
6SS	0.002	0.011
6NP	0.012	0.036
SS support	0	0
NP support	0	0

The amount of N_2O formation is larger than NO desorption amount could be owing to strong interaction between NO molecule and SS and NP samples.

NH$_3$-TPD

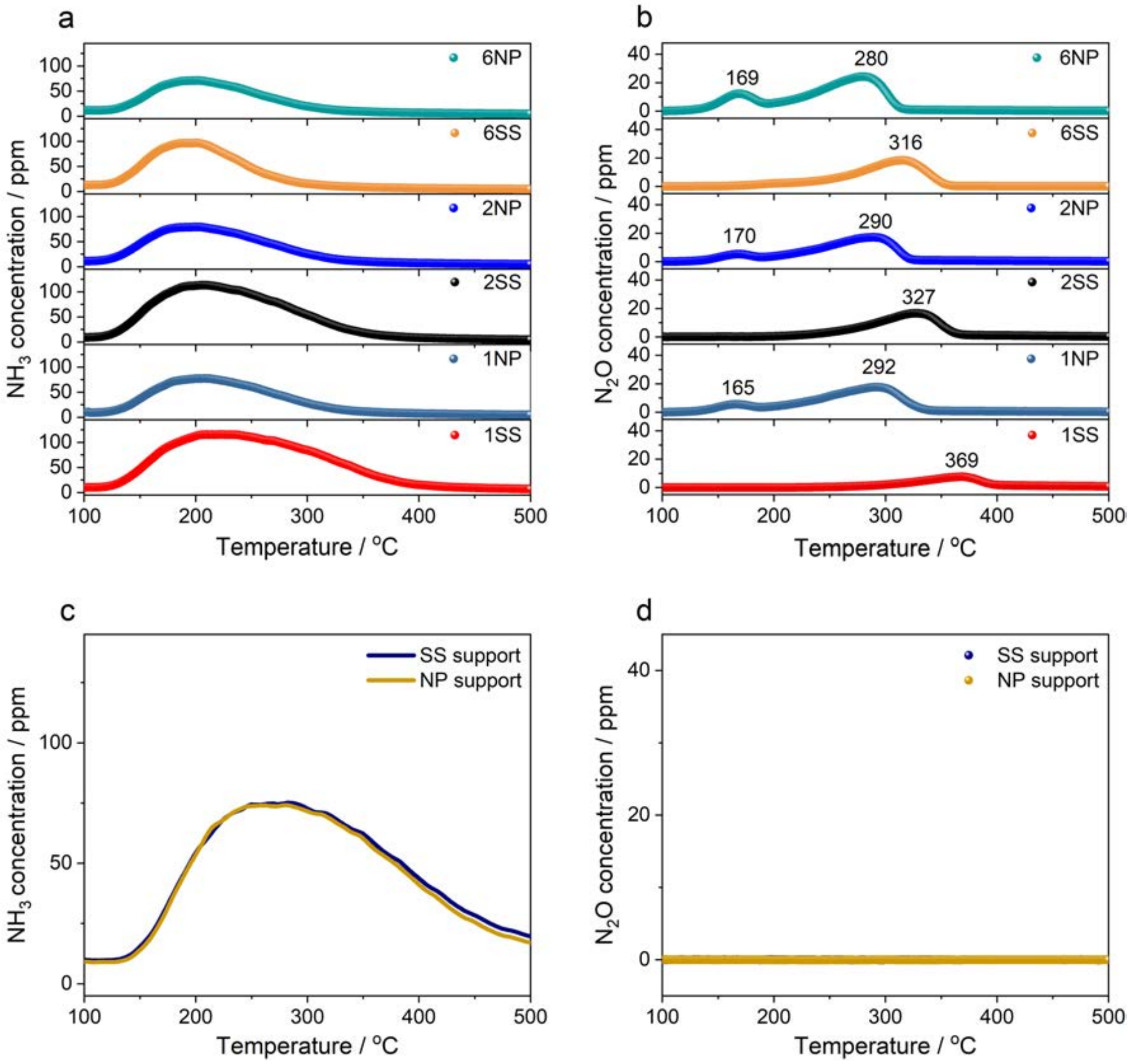

Supplementary Figure 23. Acidity evaluation by NH$_3$-TPD. (a) NH$_3$ desorption profiles as a function of temperature for 1SS, 1NP, 2SS, 2NP, 6SS and 6NP. (b) the N$_2$O formation during NH$_3$ desorption for 1SS, 1NP, 2SS, 2NP, 6SS and 6NP. (c) NH$_3$ desorption profiles for SS support and NP support. (d) N$_2$O desorption profiles for SS support and NP support.

Supplementary Table 8. Desorption amount of NH_3 and N_2O during NH_3-TPD measurement.

Sample	NH_3 desorption amount / mmol / g	N_2O formation amount / mmol / g
1SS	0.311	0.007
1NP	0.156	0.020
2SS	0.259	0.020
2NP	0.148	0.026
6SS	0.148	0.024
6NP	0.119	0.037
SS support	0.223	0
NP support	0.224	0

Supplementary Note 5. Catalytic performance of SS and NP in NH_3-SCR of NO reaction.

Across the full temperature range, all SS samples consistently exhibited significantly lower N_2O selectivity compared to the NP samples (**Supplementary Fig. 24**). For 1SS, 1NP, 2SS and 2NP samples, 1SS and 2SS samples showed higher NO conversion than 1NP and 2NP samples at high temperature ranges (from 300 ^{o}C or 250 ^{o}C to 400 ^{o}C), while the NP samples outperformed the SS samples in NO conversion at lower temperatures (from 150 ^{o}C to 300 ^{o}C or 250 ^{o}C). This enhanced low-temperature activity is likely attributed to the stronger oxidation ability of MnO_x nanoparticles, which facilitates the formation of reactive -NH_x intermediates from NH_3, thus accelerating subsequent reactions with NO.

For 6SS and 6NP samples, the proportion of MnO_x nanoclusters in both samples gradually increased with the Mn loading increasing to ~ 6 wt%, this lead to the enhancement of their oxidation ability. The 6SS sample thus showed higher N_2O selectivity and improved NO conversion at low temperatures compared to 1SS and 2SS samples. In contrast, 6NP sample contained more aggregation of MnO_x species as confirmed by previous HAADF-STEM-EDX results. This structural feature led to a sharp increase in N_2O selectivity in comparison to 6SS sample.

Additionally, both SS support and NP support showed negligible NO conversion (< 5%) at high temperatures, indicating catalytic activity in NH_3-SCR mainly originates from the Mn species.

NH_3-SCR of NO reaction

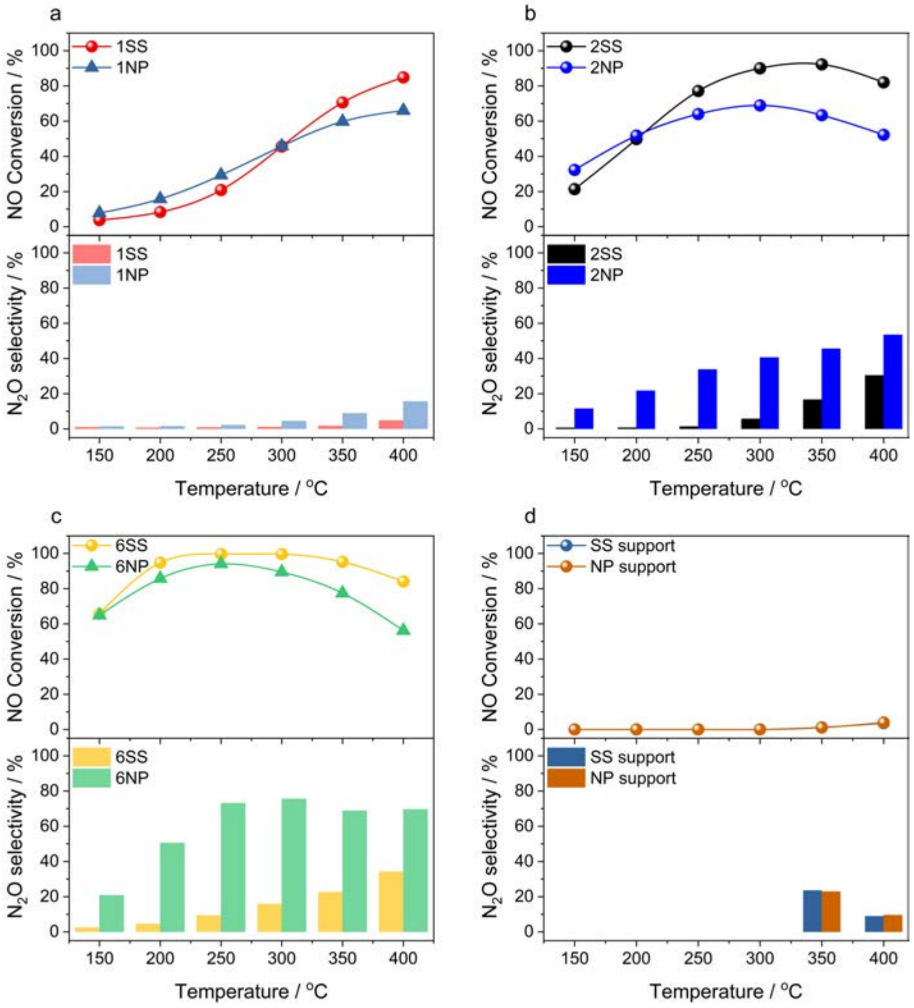

Supplementary Figure 24. Catalytic performance of SS and NP samples in NH_3-SCR of NO reaction. (a-d) NO conversion (upper panels) and N_2O selectivity (lower panels) over 1SS and 1NP (a), 2SS and 2NP (b), 6SS and 6NP (c), and SS support and NP support (d). Reaction conditions: 0.075 g catalyst, 0.1 Mpa, 150-400 °C, 5 % O_2, the concentration ratio of NH_3 : NO = 1.1:1, 333 ml /min total flow rate, 40000 h^{-1} GHSV.

Supplementary Table 9. Comparison of state-of-the-art supported catalysts for NH_3-SCR of NO at 300 °C and 250 °C.

Catalyst	Active element	Loading / wt%	NO conversion activity of each active atom per gram / 10^{-3} 300 °C	NO conversion activity of each active atom per gram / 10^{-3} 250 °C	WHSV / h^{-1} g^{-1}	Reference
2SS	Mn	1.99	3.694	3.165	266400	This work
2NP	Mn	1.94	2.900	2.694	266400	This work
6SS	Mn	5.57	1.460	1.462	266400	This work
6NP	Mn	5.93	1.232	1.296	266400	This work
Mn/TiO_2	Mn	5.0	0.331	0.202	54000	12
$Co-Mn/TiO_2$	Mn	5.0	0.353	0.232	54000	12
$Mn-Fe/TiO_2$	Mn	18.7	1.246	1.075	360000	13
V/TiO_2	V	0.8	2.759	1.839	45000	14
$V_2O_5-WO_3/TiO_2$	V	3.0	2.616	1.308	240000	15
Cu-SSZ-13	Cu	4.1	2.443	2.044	300000	16
Cu-SAPO-34	Cu	4.0	2.368	2.188	300000	16

Mo/CeO_2	Mo	21.8	0.062	0.062	40000	17
Mo/TiO_2	Mo	19.4	0.146	0.079	72000	18
W/CeO_2	W	5	0.809	0.736	60000	19
W/TiO_2	W	5	0.679	0.507	60000	19
Mn-Ce-Ti	Mn	14	0.474	0.427	237154	9
Ce/TiO_2	Ce	53	0.129	0.089	237154	9

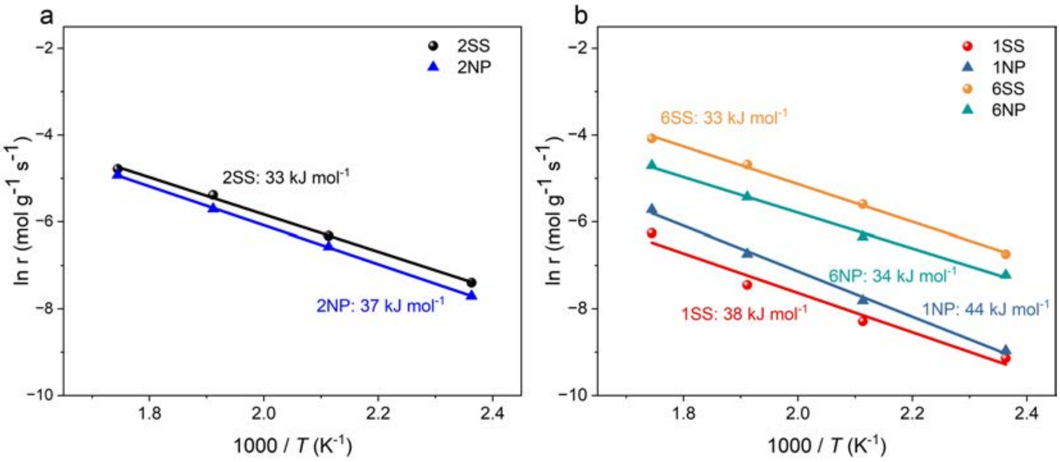

Supplementary Figure 25. Arrhenius plots of SS and NP samples in NH_3-SCR of NO reaction. (a) 2SS, 2NP. (b) 1SS, 1NP, 6SS and 6NP.

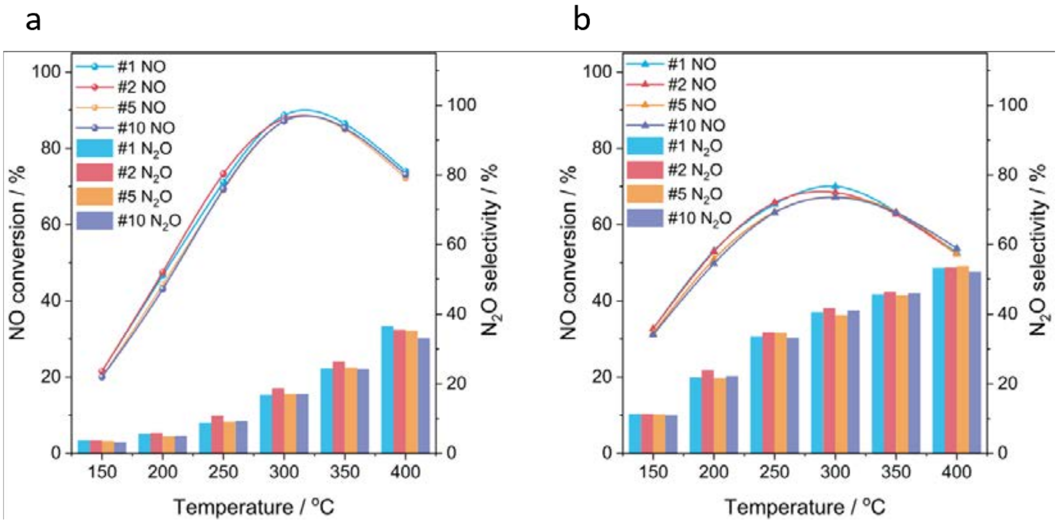

Supplementary Figure 26. Stability test of catalytic performances for 2SS (a) and 2NP (b) samples in NH_3-SCR of NO reaction. The number #1 means the first-time test. To verify the stability, ten times (5 cycles) were performed, each cycle consisting of temperature ramps from 400 °C to 150 °C and back from 150 °C to 400 °C.

After 5 cycles (ten times) measurement, the NO conversion and N_2O selectivity of 2SS and 2NP samples were stable.

Supplementary Note 6. The N_2O formation difference in SS and NP samples.

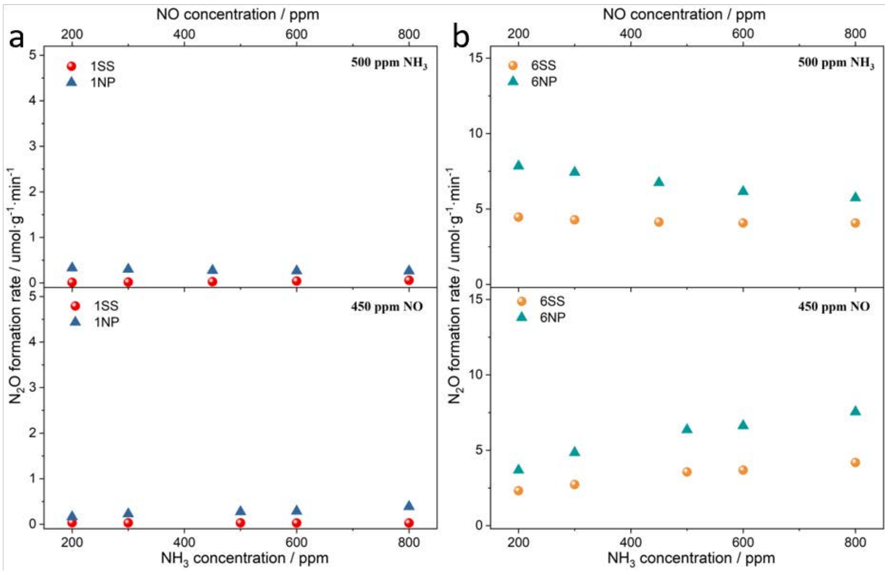

Supplementary Figure 27. Relationship between N_2O formation rate and gas partial pressure (NH_3 and NO) for 1SS, 1NP, 6SS and 6NP samples at 150 °C. (a) N_2O formation rate as the function of gas concentration for 1SS and 1NP (upper part is varying NO concentration with NH_3 fixed at 500 ppm, lower part is varying NH_3 concentration with NO fixed at 450 ppm. (b) N_2O formation rate as the function of gas concentration for 6SS and 6NP (upper part is varying NO concentration with NH_3 fixed at 500 ppm, lower part is varying NH_3 concentration with NO fixed at 450 ppm.

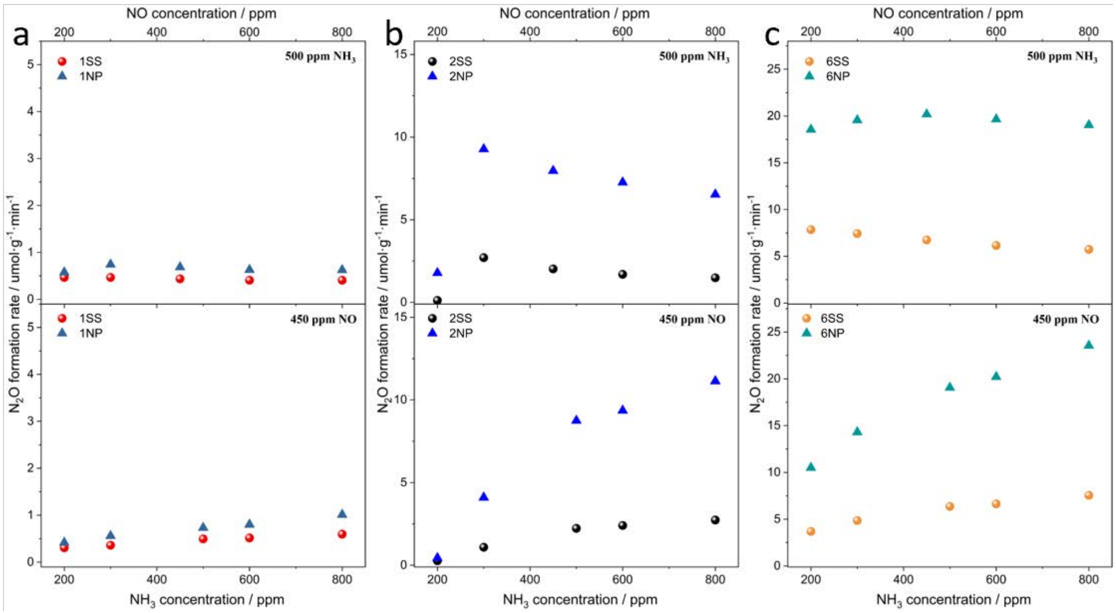

Supplementary Figure 28. Relationship between N_2O formation rate and gas partial pressure (NH_3 and NO) for SS and NP samples at 250 °C. The N_2O formation rate as a function of gas concentration (upper part is varying NO concentration with NH_3 fixed at 500 ppm, lower part is varying NH_3 concentration with NO fixed at 450 ppm for (a) 1SS and 1NP, (b) 2SS and 2NP, (c) 6SS and 6NP.

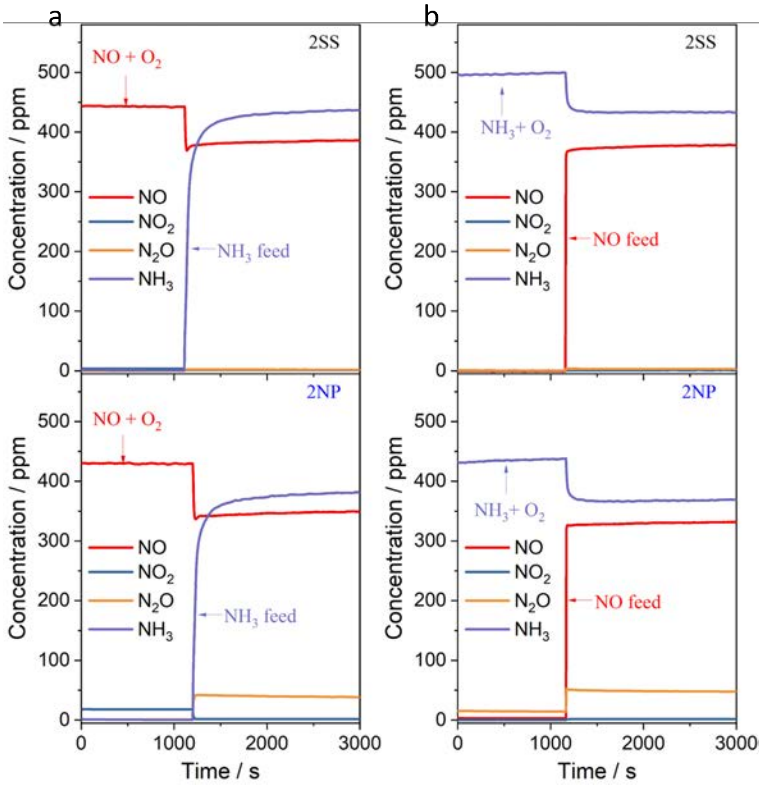

Supplementary Figure 29. Transient steady experiment in NH_3-SCR of NO reaction. (a) transient steady experiment of NH_3 feed on NO oxidation at 250 °C for 2SS (upper part) and 2NP (lower part) samples, 500 ppm NH_3 was introduced after the steady status of NO oxidation. (b) transient steady experiment of NO feed on NH_3 oxidation at 250 °C of 2SS (upper part) and 2NP (lower part), 450 ppm NO was introduced after the steady status of NH_3 oxidation. The initial feed gas condition is 450 ppm NO, 500 ppm NH_3 and 5 % O_2 when applicable.

In these transient steady experiments, NO+O_2 or NH_3+O_2 were fed to the system until reaching steady state, followed by the introduction of 500 ppm NH_3 or 450 ppm NO, respectively. When NO+O_2 were introduced, no N_2O formation was detected in any of the samples, ruling out the possibility of N_2O generation via the NO disproportionation pathway. However, upon the introduction of NH_3, approximately 39 ppm N_2O was detected for the 2NP sample, while only ~ 2 ppm was formed in the 2SS sample. After initial introduction of NH_3 and O_2 followed by NO, the N_2O concentration in the 2NP sample increased from 14 ppm to 49 ppm. In contrast, the N_2O concentration in the 2SS sample increased only slightly from 1 ppm to 3 ppm.

Supplementary Note 7. The *in situ* DRIFTS study of 2SS and 2NP samples.

The vibrational band assignments relevant to this study are summarized in **Supplementary Table 10**. *In situ* DRIFTS experiments involving pre-adsorption of NO and O_2 followed by NH_3 introduction at 150 °C were conducted on both 2SS and 2NP samples (**Supplementary Fig. 32**). Upon NH_3 exposure, the band located at ~ 1606 cm^{-1}, ~ 1582 cm^{-1}, ~ 1244 cm^{-1} and ~ 1498 cm^{-1}, which are assigned to bridged nitrate, bidentate nitrate and monodentate nitrate species, respectively, gradually diminished as the reaction proceeded. Simultaneously, new bands emerged at ~ 1598 cm^{-1}, ~ 1565 cm^{-1}, ~ 1178 cm^{-1}, along with broad features in the N-H stretching region (3100 cm^{-1} ~ 3400 cm^{-1}), indicating the formation of adsorbed N-H species. Both 2SS and 2NP samples exhibited comparable evolution profiles of these intermediate species.

To further clarify the roles of NH_3, NO and O_2, complementary *in* situ DRIFTS experiments were conducted, including NO + O_2 adsorption, NH_3 desorption and NO + O_2 desorption (**Supplementary Figs. 33-35**). During NO + O_2 adsorption (**Supplementary Fig. 33**), an additional band assigned to monodentate nitrate (~ 1283 cm^{-1}) were observed on 2NP compared to 2SS, suggesting a higher nitrate adsorption capacity compared to 2SS, consistently with the NO-TPD results. NH_3 desorption was monitored from 50 °C to 400 °C by combining DRIFTS and mass spectrometry (MS) (**Supplementary Fig. 34**), which could further track the N_2O formation during this process. Notably, 2NP generated a higher N_2O signal than 2SS during NH_3 desorption, further confirming that Mn nanoclusters could produce more N_2O. Furthermore, during the NO + O_2 desorption process, both samples showed similar changes in the bands corresponding to surface nitrates (~ 1244 cm^{-1}, ~ 1582 cm^{-1}, and ~ 1606 cm^{-1}) (**Supplementary Fig. 35**), indicating comparable interactions with NO + O_2.

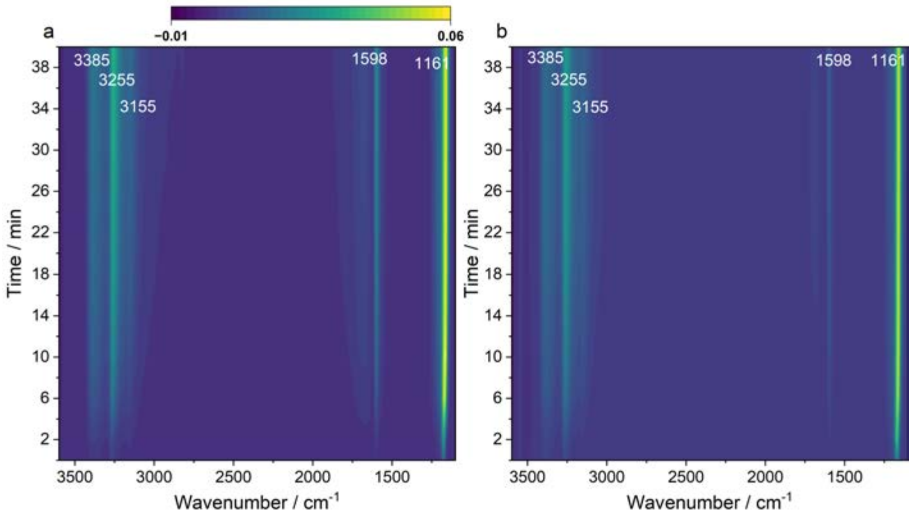

Supplementary Figure 30. *In situ* DRIFTS spectra of NH_3 adsorption on 2SS (a) and 2NP (b) measured at 150 ^{o}C.

The band at ~ 1598 cm^{-1} was assigned to asymmetric bending vibrations of the N-H bonds in NH_3 coordinately linked to Lewis acid sites. The band at ~ 1161 cm^{-1} corresponds to the symmetric bending vibration of NH_3 chemisorbed on Lewis acid sites. The bands at ~ 3385 cm^{-1} , ~ 3255 cm^{-1} and ~ 3155 cm^{-1} were attributed to the N-H stretching region.

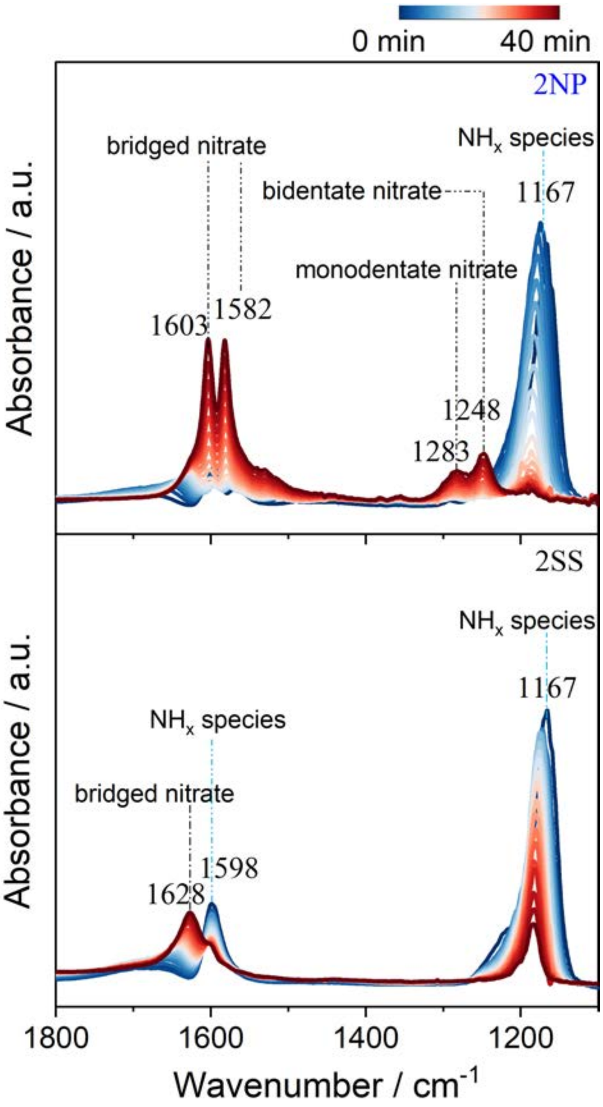

Supplementary Figure 31. Evolution of intermediate species upon introducing NO and O_2 after NH_3 pre-adsorption on 2SS and 2NP samples, monitored by *in situ* DRIFTS at 150 °C. NO + O_2 feed over the 2SS (lower part) and 2NP (upper part) samples after pre-adsorbed NH_3 at 150 °C, respectively.

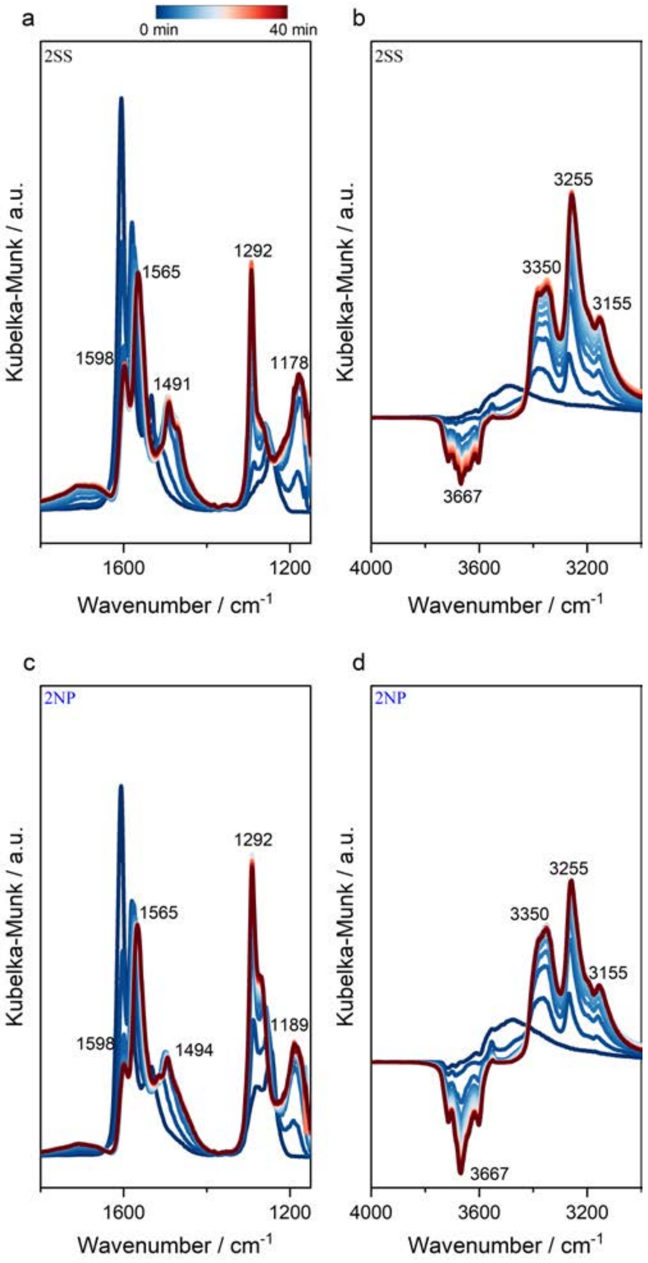

Supplementary Figure 32. Additional insights into the evolution of reaction intermediates, obtained from *in situ* DRIFTS experiment at 150 °C. (a-b) NH_3 feed over the 2SS in the low wavenumber region (a) and high wavenumber region (b) after pre-adsorbed NO plus O_2 at 150 °C. (c-d) NH_3 feed over the 2NP in the low wavenumber region (c) and high wavenumber region (d) after pre-adsorbed NO plus O_2 at 150 °C.

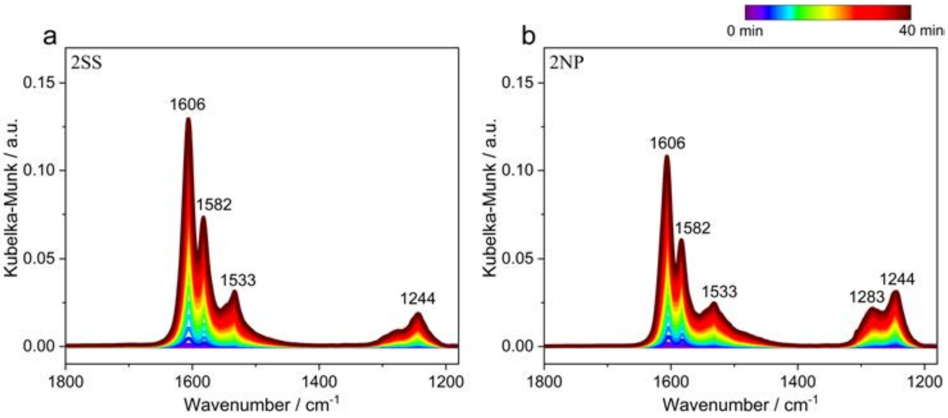

Supplementary Figure 33. ***In situ*** **DRIFT spectra of NO + O_2 adsorption on 2SS (a) and 2NP (b) at 150 °C**.

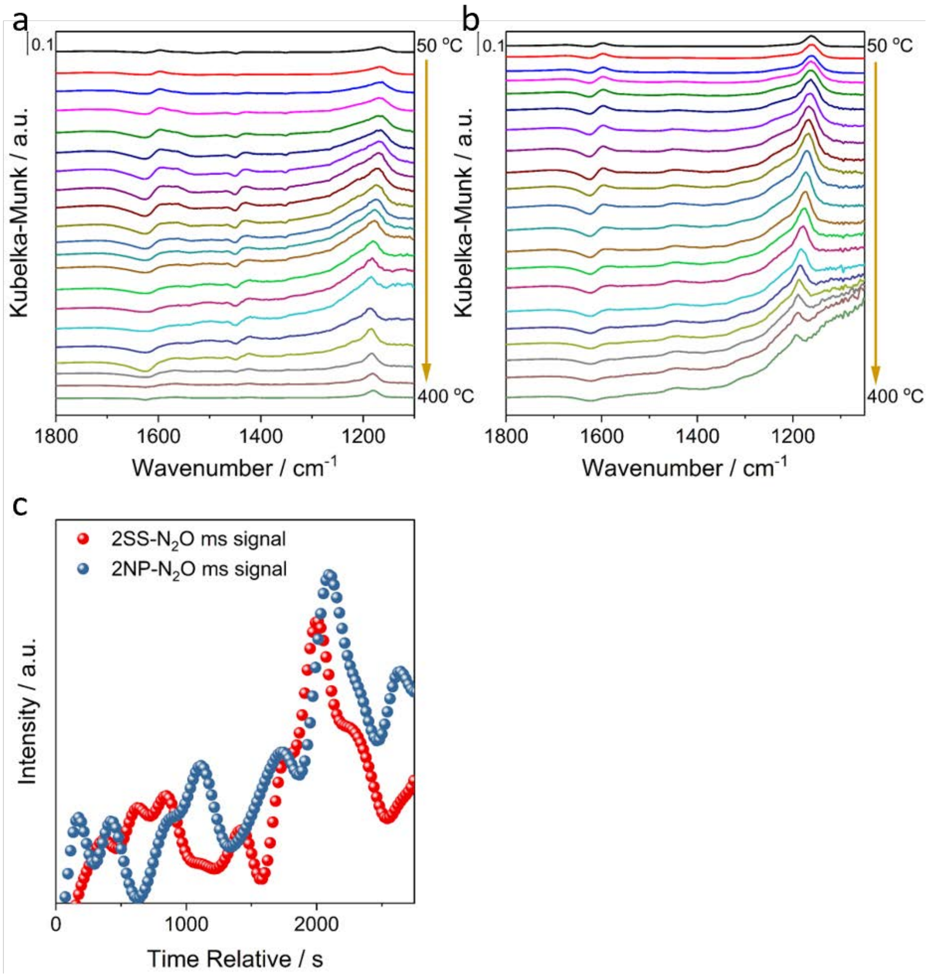

Supplementary Figure 34. ***In situ*** **DRIFT spectra of NH_3 desorption for 2SS (a) and 2NP (b), and MS signal of N_2O during desorption from 50 °C to 400 °C (c).**

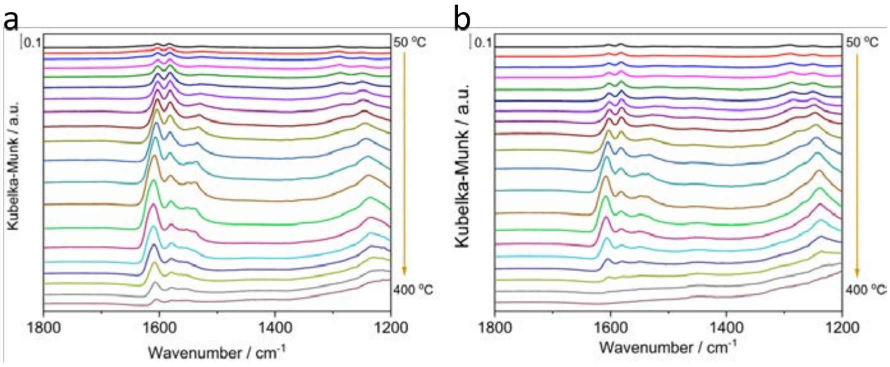

Supplementary Figure 35. *In situ* DRIFT spectra of NO + O_2 desorption for 2SS (a) and 2NP (b), measured from 50 °C to 400 °C.

Supplementary Table 10. Assignment of *in situ* DRIFTs wavelengths for surface species during measurement.

Surface species	Wavenumber (cm^{-1})	References
N-H species	~ 1598 cm^{-1}, ~ 1182 cm^{-1} and ~ 1224 cm^{-1}: Asymmetric and symmetric bending vibrations of the N-H bonds in NH_3 coordinately linked to Lewis acid sites.	20 21
	~ 1161 cm^{-1} and ~ 1167 cm^{-1}: Symmetric bending vibration of NH_3 chemisorbed on Lewis acid sites.	22 23 24
	~ 1178 cm^{-1}: the symmetric bending vibrations of coordinated NH_3 bound to Lewis acid sites.	25
	~ 1189 cm^{-1}: NH_3 coordinated with Lewis acid sites.	26
	~ 1565 cm^{-1}: $-NH_2$ species.	27 28
	~ 1491 cm^{-1} to ~ 1494 cm^{-1}: N-H bending vibration of adsorbed NH_3 species.	29
	~ 3385 cm^{-1}, ~ 3350 cm^{-1}, ~ 3255 cm^{-1} and ~ 3155 cm^{-1}: N-H stretching region.	30 31 32 33

		21 34
Nitrate species	~ 1283 cm^{-1}: monodentate nitrate.	35
	~ 1244 cm^{-1} and ~ 1248 cm^{-1}: bidentate nitrate.	36 37
	~ 1268 cm^{-1}: bidentate nitrate.	26
	~ 1292 cm^{-1}: nitrito species.	38 27 39
	~ 1498 cm^{-1}: monodentate nitrate.	40
	~ 1533 cm^{-1}: monodentate nitrates.	41 42
	~ 1582 cm^{-1}: bridging nitrate.	36
	~ 1603 cm^{-1} and ~ 1606 cm^{-1}: bridged nitrate.	22, 36
	~ 1628 cm^{-1}: bridged nitrate.	43
O-H group	~ 3667 cm^{-1}: OH-stretching bands.	44 45

Supplementary Note 8. The dependency of SS and NP samples towards different gases (NO and NH$_3$) partial pressure in NH$_3$-SCR of NO reaction.

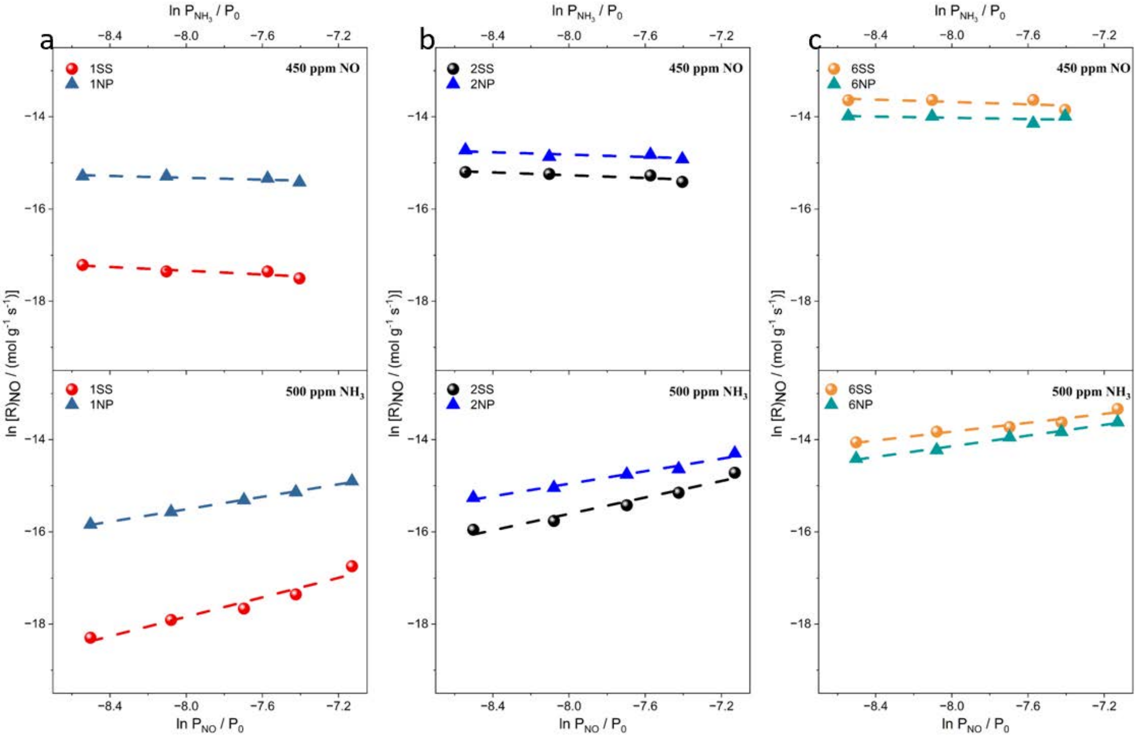

Supplementary Figure 36. Dependency of NH$_3$-SCR activity on NO and NH$_3$ concentrations for SS and NP samples at 150 °C. (a-c) upper part is varying NH$_3$ concentration with NO fixed at 450 ppm, lower part is varying NO concentration with NH$_3$ fixed at 500 ppm for 1SS, 1NP (a), 2SS, 2NP (b), 6SS and 6NP (c).

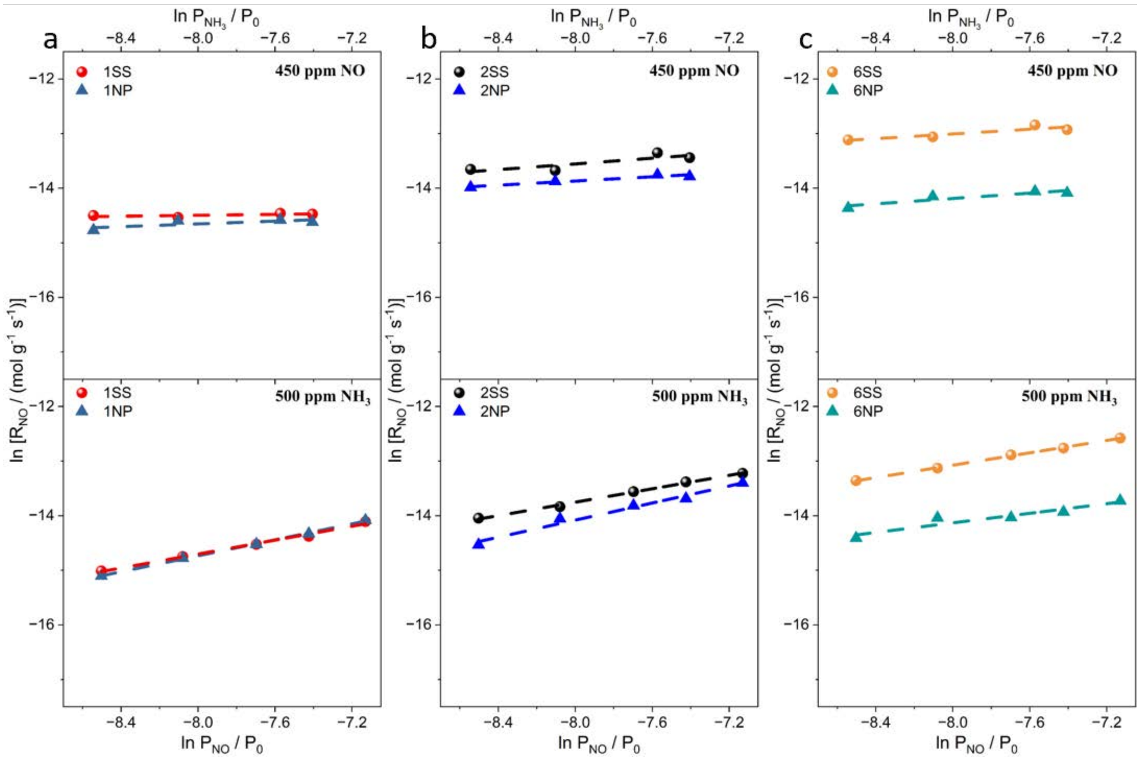

Supplementary Figure 37. Dependency of NH_3-SCR activity on NO and NH_3 concentrations for SS and NP samples at 250 ºC. (a-c) upper part is varying NH_3 concentration with NO fixed at 450 ppm, lower part is varying NO concentration with NH_3 fixed at 500 ppm for 1SS, 1NP (a), 2SS, 2NP (b), 6SS and 6NP (c).

Supplementary Table 11. Comparison of reaction order for SS and NP samples in NH_3-SCR of NO reaction at 150 ^oC and 250 ^oC, calculated based on the above dependency of NH_3-SCR activity on NO and NH_3 concentrations.

Temperature **Samples**	150 ^oC		250 ^oC	
	NO reaction order	NH_3 reaction order	NO reaction order	NH_3 reaction order
1SS	1	0	0.6	0
1NP	0.7	0	0.7	0
2SS	0.9	0	0.6	0.2
2NP	0.7	0	0.8	0.2
6SS	0.5	0	0.6	0.2
6NP	0.6	0	0.4	0.2

Supplementary Note 9. NH_3 oxidation reaction of SS and NP samples.

The SS and NP samples were evaluated for their catalytic performance in NH_3 oxidation. Across the whole temperature range, NP samples exhibited higher N_2O selectivity than SS samples. This behavior correlates with their stronger oxidation ability toward NH_3, as evidenced by the higher NH_3 conversion observed for both 1NP and 2NP compared to 1SS and 2SS (**Supplementary Fig. 38a** and **Supplementary Fig. 38b**). Generally, to better compare the N_2O selectivity, the NH_3 conversion should be maintained at similar levels. Accordingly, in the case of 6SS and 6NP samples (**Supplementary Fig. 38c)**, both samples showed comparable NH_3 conversion from 300 °C to 400 °C, whereas the N_2O selectivity of 6NP was significantly higher than that of 6SS, further highlighting the crucial role of Mn species with closer proximity in promoting N_2O formation in NH_3 oxidation reaction. In addition, SS support and NP support were also tested independently. Both exhibited negligible activity, with less than 5 % NH_3 conversion observed only at 400 °C (**Supplementary Fig. 38d**), indicating that the TiO_2 support itself contributed minimally to the observed catalytic performance.

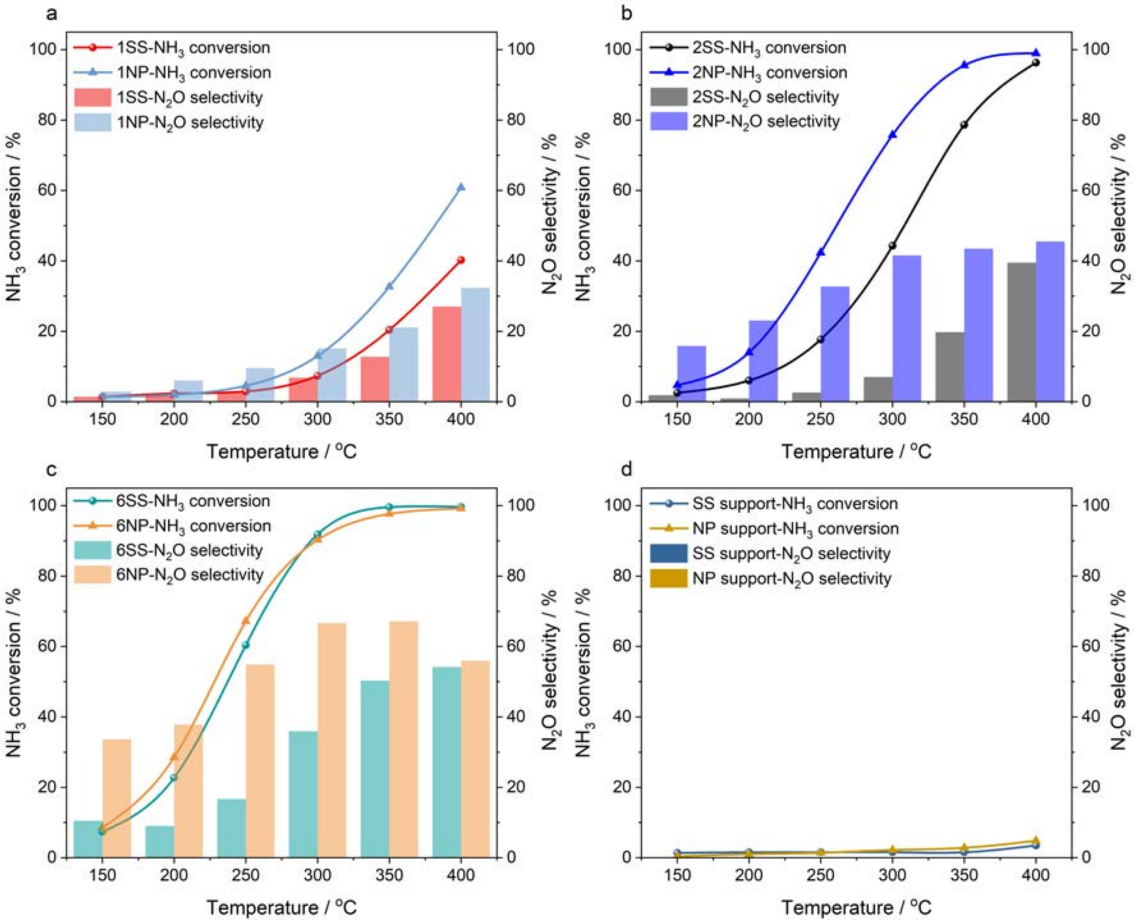

Supplementary Figure 38. Catalytic performance of SS and NP samples in NH_3 oxidation. (a-d) NH_3 oxidation over SS and NP samples. (a-c) Comparison between SS and NP catalysts with different metal loadings: 1SS vs 1NP (a), 2SS vs 2NP (b), and 6SS vs 6NP (c). (d) Comparison between SS support and NP support. Reaction conditions: 0.075 g catalyst, 0.1 Mpa, 150-400 °C, 5 % O_2, 500 ppm NH_3, 333 ml /min total flow rate, 40000 h^{-1} GHSV.

Supplementary Note 10. The characterization and catalytic performance of Ni SS, Ni NP, Co SS and Co NP samples in NH_3-SCR of NO reaction.

First, the oxidation states of Ni and Co in the corresponding samples were mainly evaluated by XANES at the Ni K-edge and Co K-edge, respectively (**Supplementary Fig. 39**). For both elements, the absorption edge energies closely matched those of NiO and CoO references, indicating that the Ni SS and Ni NP, as well as the Co SS and Co NP samples exhibit similar oxidation states (+ 2).

EXAFS was used to investigate the local coordination environments of Ni or Co sites in these samples (**Supplementary Figs. 40-44**). No metallic Ni and Co were found in Ni SS, Ni NP, Co SS and Co NP samples in the first shell compared to corresponding metal foil references, confirming the absence of metallic nanoparticles. Instead, a prominent peak at ~ 1.5 Å in the R space indicates predominant Ni-O or Co-O coordination in the first shell (**Supplementary Fig. 40**). To further distinguish the second-shell contributions from Ni-O-Ti vs Ni-O-Ni and Co-O-Ti vs Co-O-Co in the corresponding samples, wavelet transform EXAFS analysis was conducted. In general, a peak in WT EXAFS analysis at higher *k* value corresponds to scattering from heavier atom. This principle facilitates the differentiation of second-shell coordination environments. In the Ni references and samples (**Supplementary Fig. 41**), a single WT maxima at ~ 7.0 $Å^{-1}$ is observed in Ni foil, which is the characteristic of Ni-Ni interactions. In NiO, two distinct maxima appear at ~ 4.6 $Å^{-1}$ and ~ 7.0 $Å^{-1}$, corresponding to Ni-O and Ni-O-Ni scattering paths, respectively. Similarly, the 2Ni NP and 6Ni NP samples exhibit two WT maxima at ~ 4.6 $Å^{-1}$ and ~ 7.0 $Å^{-1}$, which can be attributed to Ni-O and Ni-O-Ni units, thus confirming the predominance of aggregated NiO_x. In contrast, the 2Ni SS sample shows WT maxima at ~ 4.6 $Å^{-1}$, without significant high *k* signal associated with Ni-O-Ni coordination. This suggests the absence of Ni-O-Ni interactions and supports the formation of isolated Ni single sites. The 6Ni SS sample shows a WT maximum at ~ 5.8 $Å^{-1}$, and no distinct maximum is observed around 7.0 Å^{-1}, which corresponds to the Ni-O-Ni interactions. This indicates that majority of Ni species remain isolated structures in 6Ni SS.

A similar trend is observed in the Co K-edge WT results (**Supplementary Fig. 42)**. For Co foil, a single WT maxima appears at ~ 7.0 Å^{-1}, which is the characteristic of metallic Co-Co coordination. In the CoO reference, two distinct maxima are observed at ~ 4.9 Å^{-1} and ~ 6.4 Å^{-1}, corresponding to Co-O and Co-O-Co scattering paths, respectively. The 2Co NP and 6Co NP samples exhibit similar features to CoO, with WT maxima at ~ 4.9 Å^{-1} and ~ 6.3 Å^{-1}, indicating the coexistence of Co-O and Co-O-Co coordination. These results verified that Co sites in NP samples primarily exists as aggregated CoO_x clusters. In contrast, the 2Co SS sample displays a major WT maximum at ~ 4.9 Å^{-1}, no significant high *k* signal associated with Co-O-Co coordination was detected, verifying the presence of isolated Co sites. Similarly, the 6Co SS sample exhibits a WT maximum at ~ 5.5 Å^{-1}, while no distinct maximum is observed around 6.4 Å^{-1}, suggesting that most of Co sites remain in isolated coordination environments.

EXAFS fitting provided additional information about coordination environment. For Ni samples (**Supplementary Fig. 43** and **Supplementary Table 12**), the Ni-O coordination numbers in the first shell were 5.6, 5.6, 5.2, and 4.9 for 2Ni SS, 2Ni NP, 6Ni SS, and 6Ni NP, respectively, with corresponding bond lengths of 2.03, 2.04, 2.03, and 2.05 Å. In the case of Co samples (**Supplementary Fig. 44** and **Supplementary Table 13**), the Co-O coordination numbers in the first shell were 5.0, 4.8, 4.7, and 4.6 for 2Co SS, 2Co NP, 6Co SS, and 6Co NP, respectively, with corresponding bond lengths of 1.99, 1.90, 1.94, and 1.91 Å. In the second shell, the similar backscattering amplitudes and phase shifts of Ni (or Co) and Ti make it challenging to unambiguously differentiate between Ni-Ti and Ni-Ni or Co-Ti and Co-Co contributions by quantitative EXAFS fitting. Nevertheless, the combined results from WT analysis and EXAFS confirms that Ni and Co are predominantly present as isolated sites in SS samples, whereas aggregated NiO_x or CoO_x clusters are more prevalent in NP samples.

Additionally, 2Ni SS, 2Ni NP and 6Ni SS samples were also found to be highly dispersed from the results of HAADF-STEM equipped with EDX. Whereas, NiO_x

nanoclusters (~ 20 nm) could be clearly observed in 6Ni NP sample (**Supplementary Fig. 45**). The similarity regarding the morphology of Co samples: Co nanoclusters ranging from 10 to 30 nm were predominantly found in Co NP samples, in contrast to the Co SS samples, which showed no visible Co nanoclusters (**Supplementary Fig. 46**). This confirms that Co NP samples are primarily composed of Co nanoclusters, while the Co species were highly dispersed over Co SS samples.

To further clarify the Ni structures in Ni SS, Ni NP, Co SS and Co NP samples, EPR measurements were conducted (**Supplementary Fig. 47**). For Ni samples, the sharper and more intense EPR signal observed for Ni SS sample is attributed to the distortion of TiO_2[46,47]. In contrast, Ni NP samples exhibit broader and weaker signals signifying less TiO_2 distortion. The EPR spectra of the Co samples reveal distinct differences between Co SS and Co NP structures. The 2Co SS and 6Co SS samples exhibit very weak or nearly undetectable EPR signals across the g factor range, suggesting that the Co species are predominantly present as highly dispersed single sites. These isolated Co^{2+} centers, likely located in symmetric coordination environments on the TiO_2 support, exhibit minimal magnetic interactions and may undergo spin-orbit coupling quenching, resulting in suppressed EPR intensity. In contrast, both 2Co NP and 6Co NP samples display broad and intense EPR signals centered around $g = 2.87$, which are characteristic of ferromagnetically coupled Co^{2+} species in CoO_x clusters or nanoparticles[48]. The increased signal intensity and broadening with higher Co loading in NP samples further confirm the formation of more CoO_x clusters.

Furthermore, these samples with well-defined structures were evaluated in NH_3-SCR of NO reaction (**Supplementary Fig. 48**). With the Ni or Co loading increasing from 2 wt% to 6 wt%, both Ni and Co samples exhibited enhanced NO conversion. However, SS samples consistently maintained low N_2O selectivity, whereas NP samples showed a pronounced increase in N_2O formation, especially at higher temperatures and loadings. These results verify that atomically dispersed active sites effectively suppress N_2O formation, while aggregated metal nanoclusters promote it due to closer active site proximity.

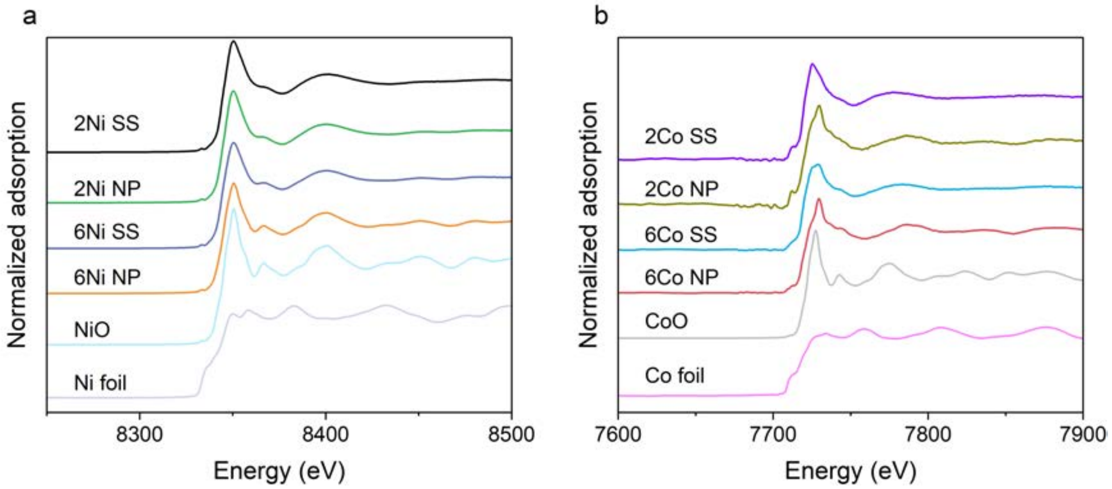

Supplementary Figure 39. Oxidation states evaluated by XANES for Ni- and Co-containing samples. (a) Normalized Ni K-edge XANES spectra of 2Ni SS, 2Ni NP, 6Ni SS, and 6Ni NP, compared with NiO and Ni foil references. (b) Normalized Co K-edge XANES spectra of 2Co SS, 2Co NP, 6Co SS, and 6Co NP, compared with CoO and Co foil references.

EXAFS

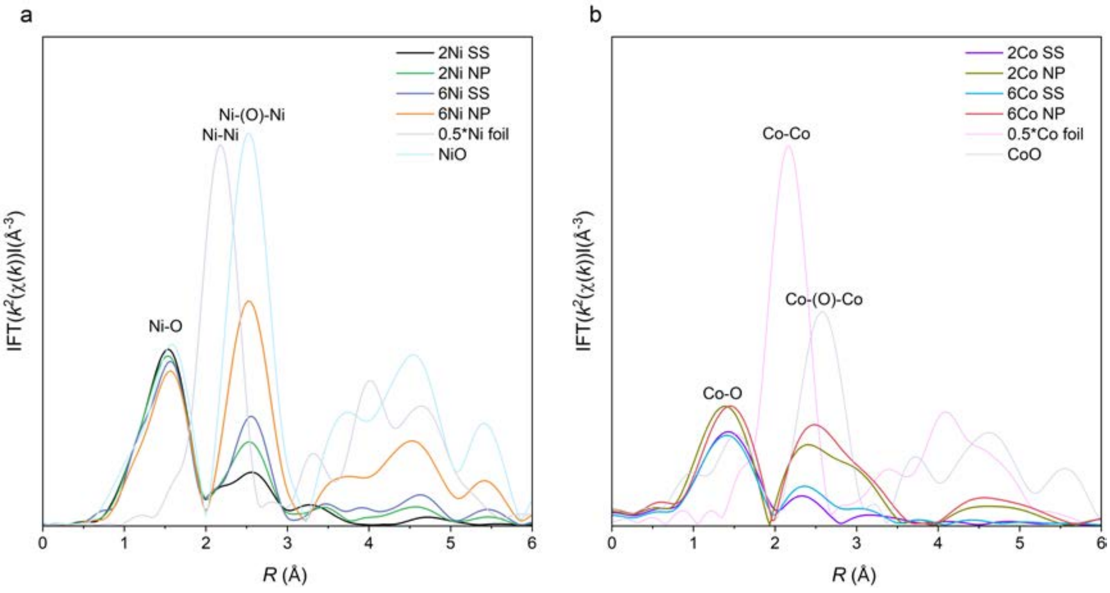

Supplementary Figure 40. Structural evidence of Ni and Co samples. (a), k^2-weighted Fourier-transformed EXAFS spectra at the Ni K-edge in R space for 2Ni SS, 2Ni NP, 6Ni SS, 6Ni NP and Ni references (Ni foil, NiO). (b), k^2-weighted Fourier-transformed EXAFS spectra at the Co K-edge in R space for 2Co SS, 2Co NP, 6Co SS, 6Co NP and Co references (Co foil, CoO).

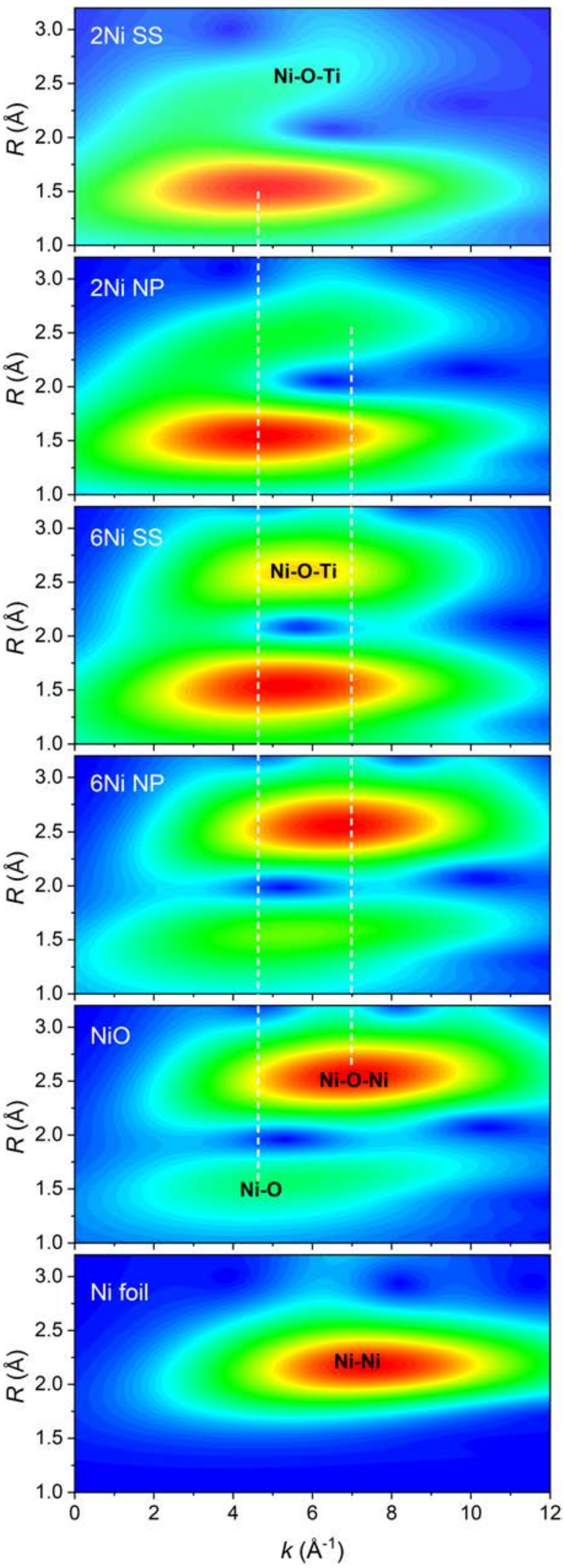

Supplementary Figure 41. Wavelet transform for k^2-weighted EXAFS signals at the Ni K-edge of Ni samples.

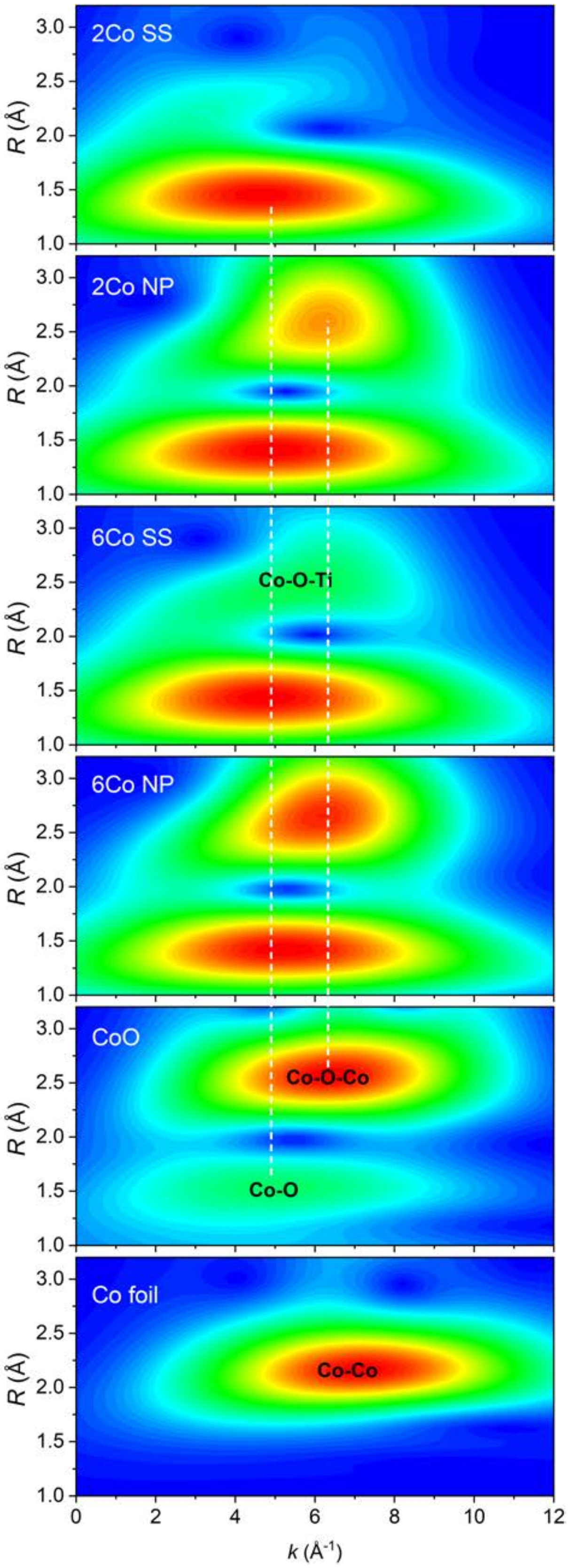

Supplementary Figure 42. Wavelet transform for k^2-weighted EXAFS signals at the Co K-edge of Co samples.

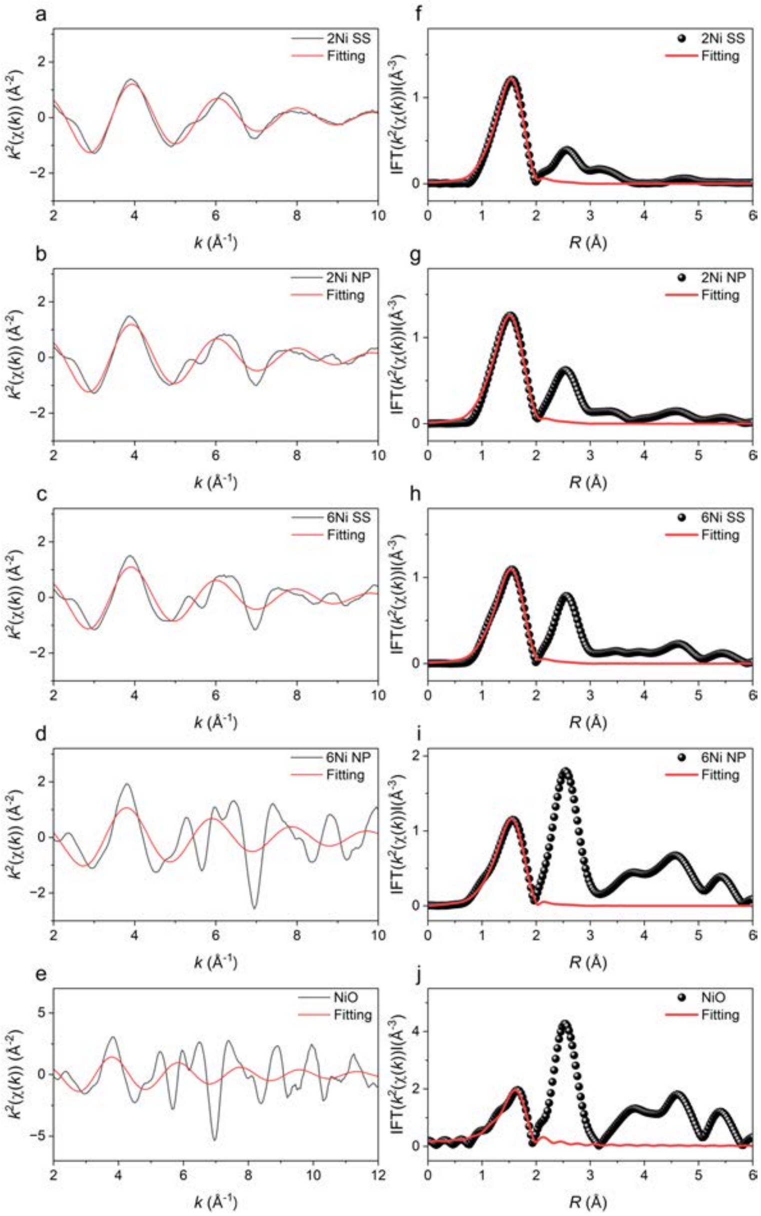

Supplementary Figure 43. k^2-weighted EXAFS spectra at the Ni K-edge for 2Ni SS, 2Ni NP, 6Ni SS, 6Ni NP and NiO. (a-e), EXAFS spectra and corresponding fittings in k space for 2Ni SS (a), 2Ni NP (b), 6Ni SS (c), 6Ni NP (d), and NiO reference (e). (f-j) Corresponding Fourier-transformed EXAFS spectra and fittings in R space for 2Ni SS (f), 2Ni NP (g), 6Ni SS (h), 6Ni NP (i) and NiO (j).

Supplementary Table 12. EXAFS fitting parameters at Ni K-edge for Ni SS, Ni NP samples and NiO reference.

Sample	Shell	CN[a]	R[b] [Å]	σ^2 [c] [$Å^2$]	R[d]-factor [%]
NiO	Ni-O	6*	2.08 ± 0.02	0.004 ± 0.002	1.9
2Ni SS	Ni-O	5.6 ± 0.4	2.03 ± 0.01	0.007 ± 0.001	0.6
2Ni NP	Ni-O	5.6 ± 0.7	2.04 ± 0.01	0.007 ± 0.002	0.6
6Ni SS	Ni-O	5.2 ± 0.6	2.03 ± 0.01	0.007 ± 0.002	0.8
6Ni NP	Ni-O	4.9 ± 0.5	2.05 ± 0.01	0.005 ± 0.001	0.6

a) CN: Coordination numbers; b) R: Bond distance; c) σ^2: Debye-Waller factors; d) R factor: The values of R factor quantify the goodness of fit when fitting all data scans for each sample. S_0^2 was fixed to 0.835 according to the experimental EXAFS fitting of NiO by fixing CN as the known crystallographic value. The fitting range of k space for relevant references and samples were as follows, NiO: 2.47 ~ 11.58 $Å^{-1}$. 2Ni SS: 2.27 ~ 12.17 $Å^{-1}$. 2Ni NP: 2.27 ~ 10.20 $Å^{-1}$. 6Ni SS: 2.27 ~ 11.64 $Å^{-1}$. 6Ni NP: 2.13 ~ 11.56 $Å^{-1}$.

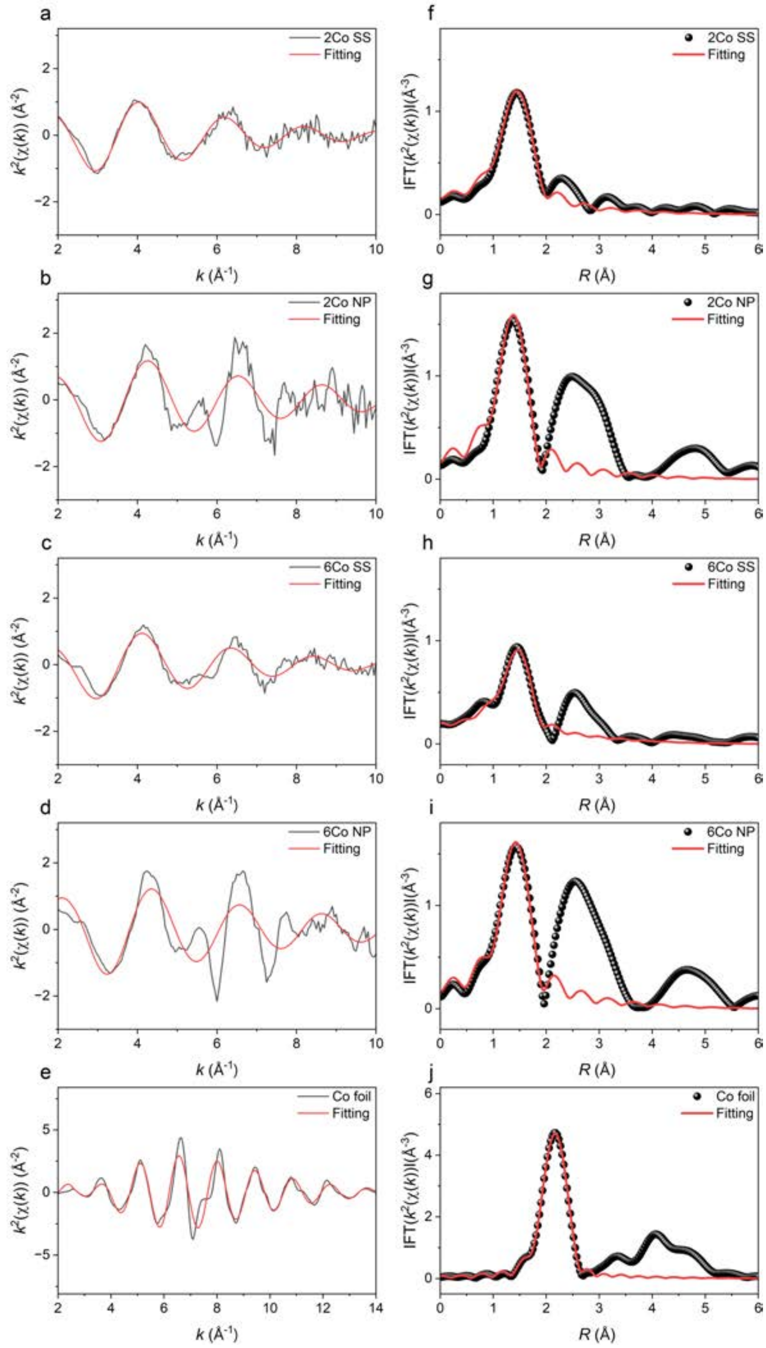

Supplementary Figure 44. k^2-weighted EXAFS spectra at the Co K-edge for 2Co SS, 2Co NP, 6Co SS, 6Co NP and Co foil. (a-e), EXAFS spectra and corresponding fittings in k space for 2Co SS (a), 2Co NP (b), 6Co SS (c), 6Co NP (d), and Co foil reference (e). (f-j) EXAFS spectra and corresponding fittings in R space 2Co SS (f), 2Co NP (g), 6Co SS (h), 6Co NP (i), and Co foil (j).

Supplementary Table 13. EXAFS fitting parameters at Co K-edge for Co SS, Co NP samples and Co foil reference.

Sample	Shell	CN[a]	R[b] [Å]	σ^{2} [c] [Å^2]	R[d]-factor [%]
Co foil	Co-Co	12*	2.49 ± 0.01	0.006 ± 0.001	0.2
2Co SS	Co-O	5.0 ± 1.0	1.99 ± 0.02	0.008 ± 0.004	1.0
2Co NP	Co-O	4.8 ± 0.8	1.90 ± 0.01	0.004 ± 0.002	0.8
6Co SS	Co-O	4.7 ± 0.5	1.94 ± 0.01	0.007 ± 0.001	0.2
6Co NP	Co-O	4.6 ± 0.8	1.91 ± 0.01	0.003 ± 0.002	0.8

a) CN: Coordination numbers; b) R: Bond distance; c) σ^2: Debye-Waller factors; d) R factor: The values of R factor quantify the goodness of fit when fitting all data scans for each sample. S_0^2 was fixed to 0.749 according to the experimental EXAFS fitting of Co foil by fixing CN as the known crystallographic value. The fitting range of k space for relevant references and samples were as follows, Fitting range: Co foil: 2.74 ~ 11.98 Å^{-1}. 2Co SS: 2.37 ~ 8.70 Å^{-1}. 2Co NP: 2.53 ~ 9.12 Å^{-1}. 6Co SS: 3.62 ~ 10.01 Å^{-1}. 6Co NP: 2.74 ~ 9.20 Å^{-1}.

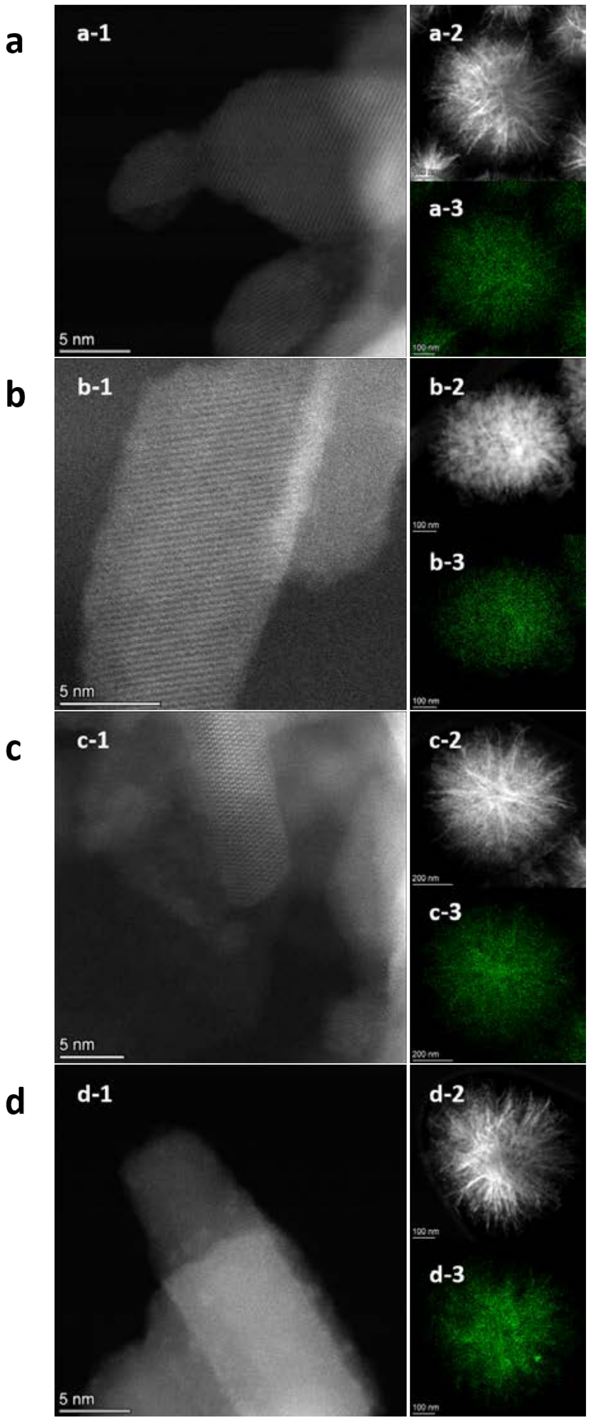

Supplementary Figure 45. Atomical structure of 2Ni SS, 2Ni NP, 6Ni SS and 6Ni NP samples characterized by HAADF-STEM. (a-d), HAADF-STEM image of 2Ni SS (a), 2Ni NP (b), 6Ni SS (c) and 6Ni NP (d) samples with corresponding EDX elemental mapping of Ni (green).

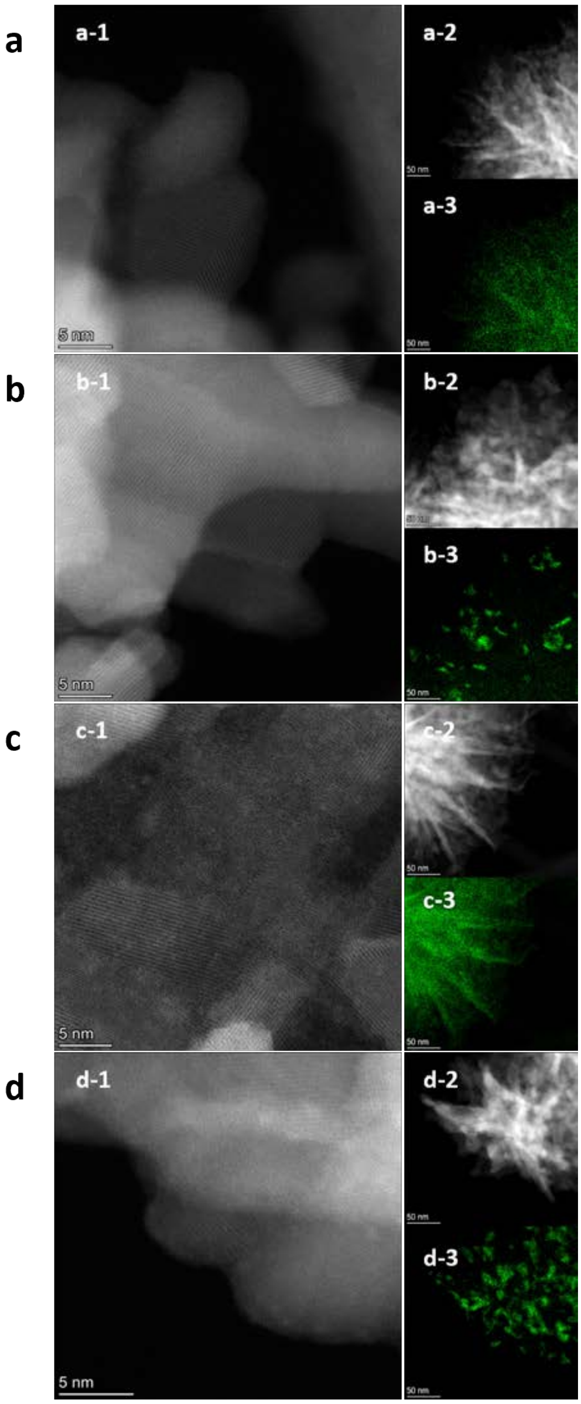

Supplementary Figure 46. Atomical structure of 2Co SS, 2Co NP, 6Co SS and 6Co NP samples characterized by HAADF-STEM. (a-d), HAADF-STEM image of 2Co SS (a), 2Co NP (b), 6Co SS (c) and 6Co NP (d) samples with corresponding EDX elemental mapping of Co (green).

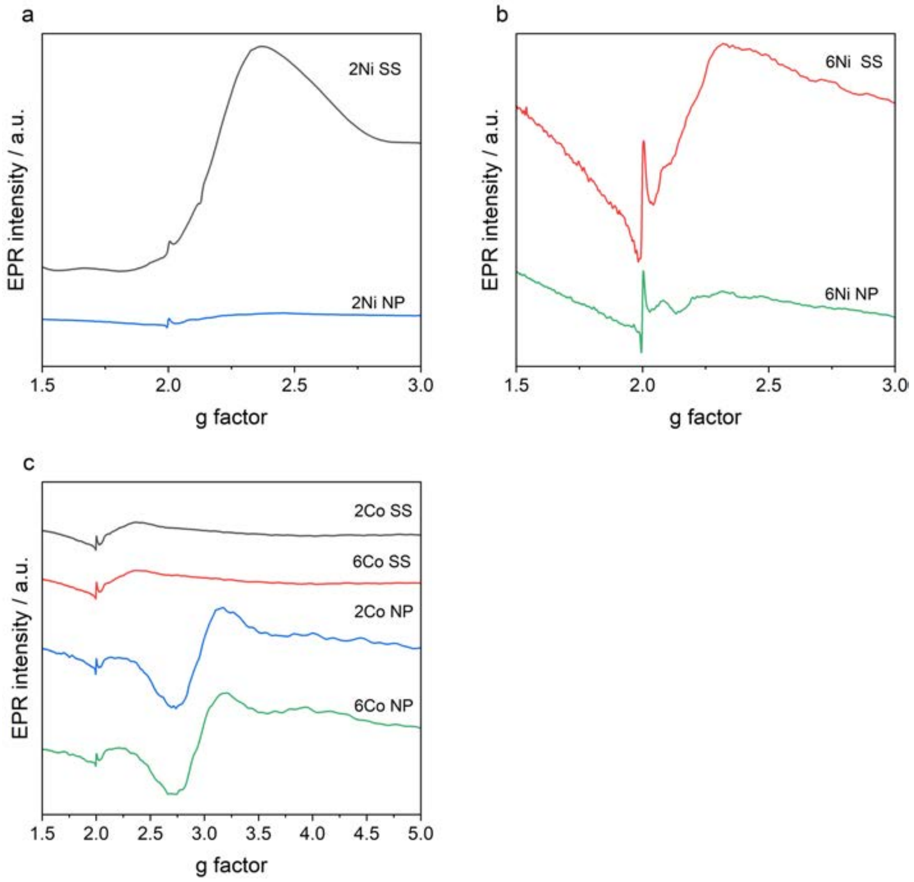

Supplementary Figure 47. EPR spectra of Ni- and Co-containing samples. (a-b) EPR spectra of Ni-based samples. (c) EPR spectra of Co-based samples.

Catalytic performance in NH_3-SCR of NO reaction of Ni SS, Ni NP, Co SS and Co NP samples

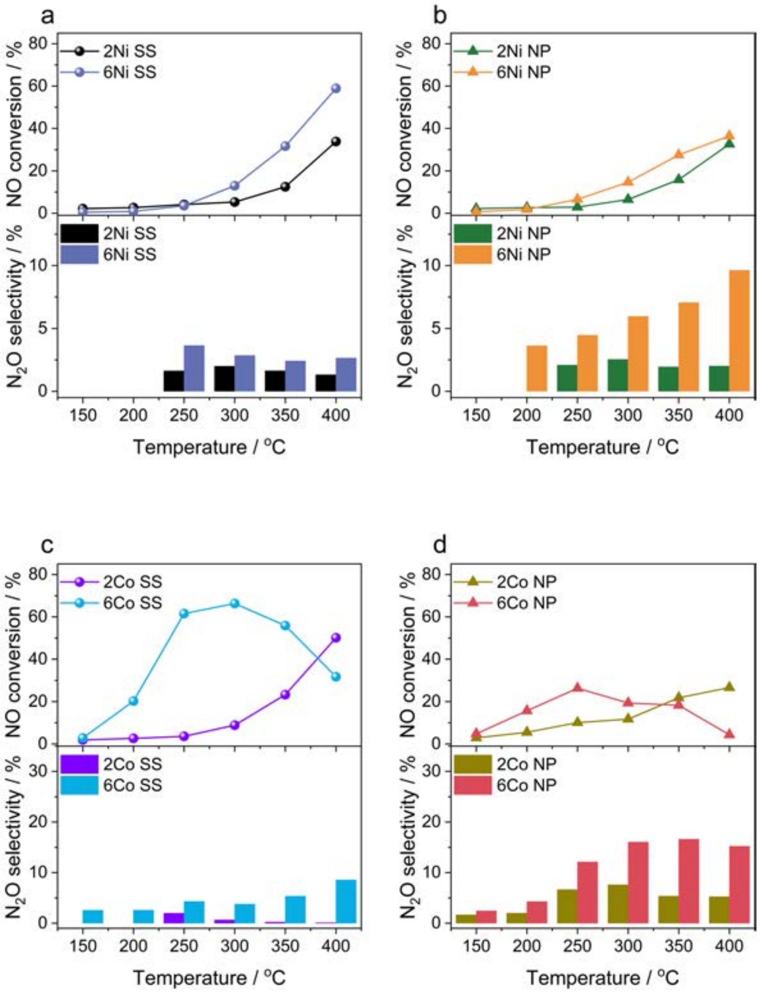

Supplementary Figure 48. Catalytic performance of Ni and Co SS and NP samples with different loadings in NH_3-SCR of NO reaction. (a) Ni SS samples, (b) Ni NP samples, (c) Co SS samples, and (d) Co NP samples. Upper panels show NO conversion versus temperature, and lower panels show N_2O selectivity versus temperature. Reaction conditions: 0.075g catalyst, 0.1 Mpa, 150-400 ºC, 5 % O_2, the concentration ratio of NH_3 : NO = 1.1:1, 333ml /min total flow rate, 40000 h^{-1} GHSV.

Supplementary References

1. Akshay, V. R., Arun, B., Mandal, G. & Vasundhara, M. Impact of Mn-dopant concentration in observing narrowing of band-gap, urbach tail and paramagnetism in anatase TiO_2 nanocrystals. *New J. Chem.* **43**, 14786–14799 (2019).
2. Hazem, R., Izerrouken, M., Cheraitia, A. & Djehlane, A. Raman study of ion beam irradiation damage on nanostructured TiO_2 thin film. *Nucl. Instrum. Methods Phys. Res. B* **444**, 62–67 (2019).
3. Zuo, S. et al. Local compressive strain-induced anti-corrosion over isolated Ru-decorated Co_3O_4 for efficient acidic oxygen evolution. *Nat. Commun.* **15**, 9514 (2024).
4. Funke, H., Scheinost, A. C. & Chukalina, M. Wavelet analysis of extended x-ray absorption fine structure data. *Phys. Rev. B* **71**, 094110 (2005).
5. Agrachev, M. *et al.* Electron paramagnetic resonance spectroscopy for the analysis of single-atom catalysts. *Chem Catalysis* **4**, 101136 (2024).
6. Kumar, C. P., Gopal, N. O., Wang, T. C., Wong, M.-S. & Ke, S. C. EPR Investigation of TiO_2 Nanoparticles with Temperature-Dependent Properties. *J. Phys. Chem. B* **110**, 5223–5229 (2006).
7. Saponjic, Z. V *et al.* Charge separation and surface reconstruction: A Mn^{2+} doping study. *J. Phys. Chem. B* **110**, 25441–25450 (2006).
8. Horn, M. & Schwerdtfeger, C. F. EPR of substitutional and charge compensated Fe^{3+} in anatase (TiO_2). *J. Phys. Chem. Solids* **32**, 2529–2538 (1971).
9. Gevers, L. E. *et al.* Unraveling the structure and role of Mn and Ce for NO_x reduction in application-relevant catalysts. *Nat. Commun.* **13**, 2960 (2022).
10. Di Castro, V. & Polzonetti, G. XPS study of MnO oxidation. *J. Electron Spectrosc. Relat. Phenom.* **48**, 117–123 (1989).
11. Chen, D. *et al.* Investigation of the role of surface lattice oxygen and bulk lattice oxygen migration of cerium-based oxygen carriers: XPS and designed H_2-TPR characterization. *Appl. Catal. B* **218**, 249–259 (2017).

12. Hu, H. *et al.* Mechanistic Aspects of deNO$_x$ Processing over TiO$_2$ Supported Co-Mn Oxide Catalysts: Structure-Activity Relationships and In Situ DRIFTs Analysis. *ACS Catal.* **5**, 6069–6077 (2015).

13. Putluru, S. S. R. *et al.* Mn/TiO$_2$ and Mn-Fe/TiO$_2$ catalysts synthesized by deposition precipitation-promising for selective catalytic reduction of NO with NH$_3$ at low temperatures. *Appl. Catal. B* **165**, 628–635 (2015).

14. Lietti, L. *et al.* Characterization and reactivity of V$_2$O$_5$-MoO$_3$/TiO$_2$ de-NO$_x$ SCR catalysts. *J. Catal.* **187**, 419–435 (1999).

15. Wang, C., Yang, S., Chang, H., Peng, Y. & Li, J. Dispersion of tungsten oxide on SCR performance of V$_2$O$_5$WO$_3$/TiO$_2$: Acidity, surface species and catalytic activity. *Chem. Eng. J.* **225**, 520–527 (2013).

16. Wang, D. *et al.* A comparison of hydrothermal aging effects on NH$_3$-SCR of NO$_x$ over Cu-SSZ-13 and Cu-SAPO-34 catalysts. *Appl. Catal. B* **165**, 438–445 (2015).

17. Chang, H. *et al.* Design Strategies for P-Containing Fuels Adaptable CeO$_2$-MoO$_3$ Catalysts for DeNO$_x$: Significance of Phosphorus Resistance and N$_2$ Selectivity. *Environ. Sci. Technol.* **47**, 11692–11699 (2013).

18. Zhang, J. *et al.* Unraveling the high catalytic activity of single atom Mo-doped TiO$_2$ toward NH$_3$-SCR: Synergetic roles of Mo as acid sites and oxygen vacancies as oxidation sites. *Chem. Eng. J.* **465**, 142759 (2023).

19. Liu, S., Wang, H., Wei, Y. & Zhang, R. Core-shell structure effect on CeO$_2$ and TiO$_2$ supported WO$_3$ for the NH$_3$-SCR process. *Mol. Catal.* **485**, 110822 (2020).

20. Qiu, L. *et al.* In situ IR studies of Co and Ce doped Mn/TiO$_2$ catalyst for low-temperature selective catalytic reduction of NO with NH$_3$. *Appl. Surf. Sci.* **357**, 189–196 (2015).

21. Tsyganenko, A. A., Pozdnyakov, D. V & Filimonov, V. N. Infrared study of surface species arising from ammonia adsorption on oxide surfaces. *J Mol Struct* **29**, 299–318 (1975).

22. Zhang, Q. *et al.* In situ DRIFTS investigation of NH$_3$-SCR reaction over CeO$_2$/zirconium phosphate catalyst. *Appl. Surf. Sci.* **435**, 1037–1045 (2018).

23. Tan, W. *et al.* Gas phase sulfation of ceria-zirconia solid solutions for generating highly efficient and SO_2 resistant NH_3-SCR catalysts for NO removal. *J. Hazard. Mater.* **388**, 121729 (2020).

24. Guo, R. *et al.* Mechanistic Investigation of the Promotion Effect of Bi Modification on the NH_3-SCR Performance of Ce/TiO_2 Catalyst. *J. Phys. Chem. C* **121**, 27535–27545 (2017).

25. Liu, Z., Liu, Y., Chen, B., Zhu, T. & Ma, L. Novel Fe-Ce-Ti catalyst with remarkable performance for the selective catalytic reduction of NO_x by NH_3. *Catal. Sci. Technol.* **6**, 6688–6696 (2016).

26. Zhao, S. *et al.* $FeVO_4$-supported Mn-Ce oxides for the low-temperature selective catalytic reduction of NO_x by NH_3. *Catal. Sci. Technol.* **11**, 6770–6781 (2021).

27. Chen, L., Li, J. & Ge, M. DRIFT Study on Cerium-Tungsten/Titiania Catalyst for Selective Catalytic Reduction of NO_x with NH_3. *Environ. Sci. Technol.* **44**, 9590–9596 (2010).

28. Li, Y. *et al.* Role of CTAB in the improved H_2O resistance for selective catalytic reduction of NO with NH_3 over iron titanium catalyst. *Chem. Eng. J.* **347**, 313–321 (2018).

29. Yang, X. *et al.* Sequential active-site switches in integrated Cu/Fe-TiO_2 for efficient electroreduction from nitrate into ammonia. *Appl. Catal. B* **325**, 122360 (2023).

30. Steinbach, C., Buck, U. & Beu, T. A. Infrared spectroscopy of large ammonia clusters as a function of size. *J. Chem. Phys.* **125**, 133403 (2006).

31. Leewis, C. M., Kessels, W. M. M., Sanden, M. C. M. van de & Niemantsverdriet, J. W. Ammonia adsorption and decomposition on silica supported Rh nanoparticles observed by in situ attenuated total reflection infrared spectroscopy. *Appl. Surf. Sci.* **253**, 572–580 (2006).

32. Liu, N., Wang, J., Wang, F. & Liu, J. Promoting effect of tantalum and antimony additives on deNO_x performance of $Ce_3Ta_3SbO_x$ for NH_3-SCR reaction and DRIFT studies. *J. Rare Earths* **36**, 594–602 (2018).

33. Yang, X. *et al.* DRIFTS study of ammonia activation over CaO and sulfated CaO for NO reduction by NH_3. *Environ. Sci. Technol.* **45**, 1147–1151 (2011).

34. Ledoux, R. L. & White, J. L. Infrared studies of hydrogen bonding interaction between kaolinite surfaces and intercalated potassium acetate, hydrazine, formamide, and urea. *J. Colloid Interface Sci.* **21**, 127–152 (1966).

35. Yang, J. *et al.* In situ IR comparative study on N_2O formation pathways over different valence states manganese oxides catalysts during NH_3–SCR of NO. *Chem. Eng. J.* **397**, 125446 (2020).

36. Zhan, S. *et al.* Efficient NH_3-SCR removal of NO_x with highly ordered mesoporous $WO_3(\chi)$-CeO_2 at low temperatures. *Appl. Catal. B* **203**, 199–209 (2017).

37. Barreau, M., Tarot, M.-L., Duprez, D., Courtois, X. & Can, F. Remarkable enhancement of the selective catalytic reduction of NO at low temperature by collaborative effect of ethanol and NH_3 over silver supported catalyst. *Appl. Catal. B* **220**, 19–30 (2018).

38. Ma, Z. *et al.* Impacts of niobia loading on active sites and surface acidity in NbO_x/CeO_2–ZrO_2 NH_3–SCR catalysts. *Appl. Catal. B* **179**, 380–394 (2015).

39. Sedlmair, Ch., Seshan, K., Jentys, A. & Lercher, J. A. Elementary steps of NO_x adsorption and surface reaction on a commercial storage–reduction catalyst. *J. Catal.* **214**, 308–316 (2003).

40. Cao, F. *et al.* The activity and characterization of MnO_x-CeO_2-ZrO_2/γ-Al_2O_3 catalysts for low temperature selective catalytic reduction of NO with NH_3. *Chem. Eng. J.* **243**, 347–354 (2014).

41. Chen, J. *et al.* Synthesis of hierarchically porous Co_3O_4/Biomass carbon composites derived from MOFs and their highly NO_2 gas sensing performance. *Microporous Mesoporous Mater.* **321**, 111108 (2021).

42. Xie, S. *et al.* Low temperature high activity of M (M = Ce, Fe, Co, Ni) doped M-Mn/TiO_2 catalysts for NH_3-SCR and in situ DRIFTS for investigating the reaction mechanism. *Appl. Surf. Sci.* **515**, 146014 (2020).

43. Wang, X. *et al.* Insight into the dynamic behaviors of reactants with temperature over a TiO_x-based catalyst for NO_x removal via NH_3-SCR. *Appl. Surf. Sci.* **605**, 154689 (2022).

44. Chakarova, K. & Hadjiivanov, K. H-bonding of zeolite hydroxyls with weak bases: FTIR study of CO and N_2 adsorption on HD-ZSM-5. *J. Phys. Chem. C* **115**, 4806–4817 (2011).

45. Kloprogge, J. T., Ruan, H. D. & Frost, R. L. Thermal decomposition of bauxite minerals: infrared emission spectroscopy of gibbsite, boehmite and diaspore. *J. Mater. Sci.* **37**, 1121–1129 (2002).

46. Thamarai Selvi, E. & Meenakshi Sundar, S. Popcorn like morphology and absence of room temperature ferromagnetism in Ni doped SnO_2 nanoparticles. *J. Mater. Sci.: Mater. Electron.* **29**, 38–48 (2018).

47. Cahyaningsih, D., Taufik, A. & Saleh, R. Effect of Ni doping on the structural and optical properties of TiO_2 nanoparticles prepared by co-precipitation method. *J. Phys.: Conf. Ser.* **1442**, 012034 (2020).

48. Li, X. *et al.* Cobalt single-atom catalysts with high stability for selective dehydrogenation of formic acid. *Angew. Chem. Int. Ed.* **59**, 15849–15854 (2020).